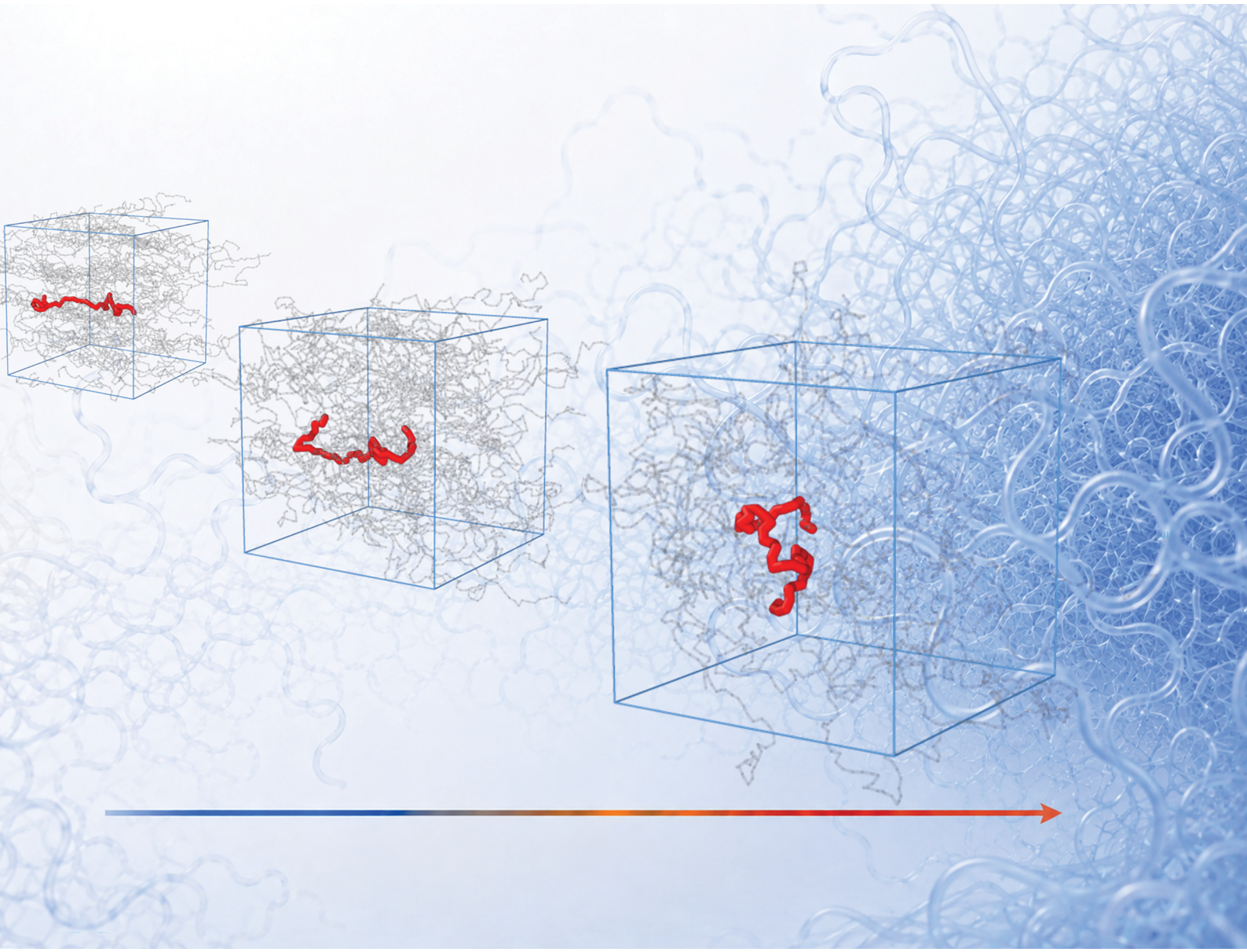
Volume 22
Number 37
30 September 2026
Pages 6183–6372

Soft Matter

rsc.li/soft-matter-journal



ISSN 1744-6848

ROYAL SOCIETY OF CHEMISTRY

PAPER
Nuofei Jiang and Evelyne van Ruymbeke
Reentanglement dynamics of a highly stretched polymer chain in fixed networks and polymer melts

Soft Matter

PAPER

Published on 03 August 2026
Licence and permissions

Check for updates

Cite this: *Soft Matter*, 2026, **22**, 6206

Reentanglement dynamics of a highly stretched polymer chain in fixed networks and polymer melts

Nuofei Jiang* and Evelyne van Ruymbeke *

Received 12th May 2026,
Accepted 1st August 2026

DOI: 10.1039/d6sm00446f

rsc.li/soft-matter-journal

The reentanglement dynamics of a polymer melt which is well entangled at equilibrium but becomes disentangled after large deformation represent a key aspect of polymer entanglement dynamics that cannot be addressed from the classic reptation model that assumes constant topological constraints. In this work, we contribute to this subject by presenting a comprehensive comparison of reentanglement dynamics between a highly stretched polymer probe in fixed networks and polymer melts containing equally stretched chains, from theoretical analysis and computer simulations. Whereas the relaxation of a polymer probe in networks can be well explained by the reptation theory, a new theoretical picture is proposed to describe the reentanglement process of a polymer melt, which predicts a relaxation pathway distinct from the network case. Nevertheless, the full recovery time in the melt remains consistent with the disentanglement time. These theoretical predictions are subsequently tested against two sets of simulations. Our single-chain Langevin simulations in networks show quantitative agreement with reptation theory for both equilibrium and reentanglement dynamics. In contrast, multi-chain melt simulations confirm qualitative differences from the network case when relaxing from a highly stretched state, consistent with our theoretical predictions. Other similarities and distinctions are examined through primitive path analysis and stress relaxation. Overall, our combined theoretical and simulation results enhance the understanding of experimental observations of reentanglement dynamics and provide new insights into out-of-equilibrium behavior across multiple time scales.

I Introduction

Flexible polymer chains in their liquid states take the configuration of random coils under thermodynamic equilibrium.[1,2] Meanwhile, polymer chains are easily elongated under external stimulations like shear or extensional flows. The relaxation of highly deformed polymers to their equilibrium configurations after removing these stimulations plays an important role in many applications. For example, in the fused filament fabrication of 3D printing, the welding time must be compatible with the relaxation time of the extruded molten polymers, where the polymer chains are highly stretched.[3–5] Otherwise, the fabricated materials may suffer from weak interfaces due to the short welding time, or they cannot retain their shapes when the welding time is too long. Another field where the relaxation dynamics are considered important is polymer crystallization.[6,7] When the polymer chains remain orientated after processing, the crystallization kinetics are significantly accelerated, and unique crystal morphologies are formed.

The stretch-to-coil dynamics of polymers in the unentangled state are described by the Rouse model or the Zimm model when hydrodynamics interaction (HI) is important. For entangled polymers, their relaxation is usually explained from the classic tube model combining the reptation motion with other mechanisms including contour length fluctuation (CLF) and constraint release (CR). Under this framework, the relaxation of a linear chain in its monodispersed melt can be considered for two different cases. In the first case, the entangled sample is relaxed after a step shear or extensional strain. Assuming that the entangled network is deformed but the density of entanglements remains unchanged, the polymer chain relaxes *via* two steps: (i) for $t \ll \tau_R$, where $\tau_R \cong \tau_0 N^2$ is the Rouse time, τ_0 is the segmental relaxation time, N is the number of Kuhn segments per chain, the primitive path (PP), which is the shortest path connecting chain ends without violating topological constraint, retracts to its equilibrium contour length along the deformed tube; (ii) for $\tau_R \ll t \ll \tau_d$, where $\tau_d \cong \tau_0 N^3 N_e^{-1} \cong \tau_R Z$ is the disentanglement time, N_e is the number of Kuhn segments per entanglement strand,

Bio and Soft Matter, Institute on Condensed Matter and Nano-science, Université Catholique de Louvain, Louvain-la-Neuve 1348, Belgium. E-mail: nuofei.jiang@uclouvain.be, evelyne.vanruymbeke@uclouvain.be

This journal is © The Royal Society of Chemistry 2026

$Z \cong N/N_e$ is the entanglement number, PP reorients *via* reptation motion until all segments have renewed their positions from the original tube. This two-step relaxation mechanism successfully explained the experimental data regarding the time-strain separability of stress relaxation moduli in the nonlinear deformation regime and predicted the damping function without any adjustable parameters.[1]

The other case to consider is chain relaxation after applying a persistent flow, then stopping it in steady state. Compared to step strain, a persistent flow can significantly break the entanglement network when the flow rate is larger than the chain stretching rate $1/\tau_R$. The elongated chains are weakly entangled with each other because the magnitude of chain overlapping is reduced. There are many direct evidences from molecular dynamics (MD) simulations showing the low entangled state after subjecting to a flow,[8] from the so-called primitive path analysis (PPA).[9,10] Besides flows, experimentally there are some other strategies to obtain a disentangled sample, like freeze-drying from dilute solutions.[11] The as-prepared polymer chains take coiled configurations in this case. Starting from a disentangled state, the stretch-to-coil transition must be coupled with the reconstruction of the entanglement network.

One useful method to investigate the reentanglement dynamics experimentally is to perform interrupted shear measurement.[12,13] That is, after the cessation of a shear flow from its steady state, the same shear field is reapplied to the sample after a particular rest time. When the rest time is short and the entanglement network has not fully reconstructed, the stress overshoot at the start-up of the second shear stage is significantly weaker than the initial overshoot observed when starting from a well-equilibrated state. The stress overshot is gradually recovered with the increase of rest time until full recovery. This protocol has been reproduced in a recent study from MD simulations.[14] The experimental data by Roland *et al.*[12,13] showed that the rest time needed for the full recovery of stress overshoot is much longer than the disentanglement time from linear viscoelasticity (LVE) measurement when it is estimated by fitting the terminal regime of linear relaxation modulus from the exponential decay function (1.5 decades longer in entangled polybutadiene (PB) solutions in the range of 17–47 entanglements, and 2 decades longer in polyisobutylene (PIB) melt of 5 entanglements). Despite the difference, it must be noted that the chain-length dependence of entanglement recovery time was found to be the same as the terminal relaxation time (scales as $N^{3.4}$).[12] In the level of a scaling argument which ignores the numerical factors, it means that the reentanglement time of a disentangled melt still agrees with that of a stretched chain in a network with fixed number of obstacles, and the reorientation of PP *via* reptation remains the governing mechanism of reentanglement. The explanation of mismatch of the time-scale magnitude is that the typical definition of relaxation time from the exponential decay function is the time scale when the stress after a linear deformation is relaxed by a factor of 1/e compared to the plateau value. On the contrary, the full recovery of entanglements corresponds to the time when the stress is almost completely relaxed.[13]

Although the full recovery of entanglements seems to agree with the equilibrium dynamics in terms of dependence on chain length, clearly the reconstruction of the entanglement network at different time scales and its reliance on molecular parameters of the material cannot be understood under the framework of the tube model. Some tube-based constitutive models for entangled polymers incorporate the change of entanglement number with deformation *via* the so-called convective constraint release (CCR) mechanism.[15–19] In the CCR models, the rate of renewing an entanglement is accelerated in a highly deformed state, and thus the disentanglement and reentanglement effects are included implicitly. Meanwhile, it is also assumed in these models that there is a constant tube diameter. Some other approaches of modelling entangled polymers, like the single-chain[20] and multi-chain[21] slip-link models, also implement entanglement dynamics with the CCR mechanism. In a later refinement of the CCR model,[22] the change of entanglement density is described explicitly and the rate of disentanglement is assumed to be proportional to the rate of CCR. However, the relationship between the instant structure of the polymer chains and the entanglement number in this model still relies on an adjustable parameter, whose physical origin remains ambiguous.

Recently, a different picture of reentanglement dynamics of polymer melts was proposed by Dolata *et al.*,[23,24] claiming that reentanglement can occur in the scale of the Rouse time τ_R. Their theoretical consideration is that the creation of entanglement are controlled by CLF of the surrounding chains, relaxing in the scale of τ_R.[23] Thus, reentanglement from a disentangled state will be accelerated, leading to a recovery faster than disentanglement time τ_d. The authors referred to MD simulation data as support of their argument, showing that the equilibrium entanglement number is recovered at around $3\tau_R$. Such fast reentanglement dynamics were also reported by Boudaghi *et al.*[25] from MD simulations. We comment here that to distinguish the Rouse time from the disentanglement time one needs to check the power-law exponent with chain length ($\tau_R \sim N^2$ while $\tau_d \sim N^3$). Those reports of fast reentanglement dynamics were then discussed by Córdoba *et al.*,[26] who observed from discrete slip-link model simulations that a fraction of entanglements are renewed by the Rouse time τ_R, but the reentanglement process finishes by the disentanglement time τ_d.

In this study, we will investigate the role of molecular environment on the reentanglement dynamics by comparing the relaxation between a highly stretched polymer chain in fixed networks and in a polymer melt of equally stretched chains. By doing so, we highlight the fact that the entanglement effect in polymer melts emerges in a self-consistent manner. This subject will be considered both theoretically and from simulations. Theoretically, we address two major questions of reentanglement process of the melts: when can we observe the onset of topological interaction if the initial configuration is fully disentangled, and how is the entangled network reconstructed in relation to the instant molecular structure of the polymer chains? To address the former question, we extend the

Lin–Nolanddi ansatz[27,28] which states that entanglement occurs when the overlap number of the polymer coils reaches a particular value (found to be around 20 from extensive experimental[29] and simulation[30] datasets). For the latter question, we refer to the idea that entanglement is determined by the effective binary contact between different chains. Then, we validate our theoretical pictures based on MD simulations. In simulations, we directly generate full stretched polymers or apply tensions on the component chains, without referring to non-equilibrium simulations with flows. This strategy allows us to decouple the relaxation mechanism from the effect of strain history. The effect of initial configurations will be discussed separately.

The rest of this work is organized as follows: in Section II, we review the prediction of the classic reptation theory in terms of the reentanglement dynamics and propose the theoretical models to describe the reentanglement of polymer melts. In Section III, we explain the simulation methods for checking the theoretical predictions. In Section IV, we present detailed analysis of our simulation data and the comparison with the theory. This includes structural recovery, primitive path evolution, and stress relaxation. The conclusions of this work are summarized in Section V.

II Theoretical models

II.1 Reentanglement dynamics of a highly stretched polymer probe in a fixed network

The current section adapts the classic reptation theory to describe the relaxation of a polymer chain in a network fixed in space. The starting point is a fully stretched chain along the x-axis whose end-to-end distance is equal to its contour length $L = Nb$, as shown in Fig. 1(a) ($t = 0$). b is Kuhn length. The mesh size of the network or the distance between the obstacles is $a \cong N_e^{1/2}b$, following the classic notations. We assume the network is filled with a Θ solvent for the polymers, causing a monomeric friction coefficient ζ_0, but no HI among segments. The corresponding segmental relaxation time is: $\tau_0 \cong \zeta_0 b^2/k_BT$.

Then, the stretched chain is expected to relax *via* the following steps, as illustrated in Fig. 1(a):

(i) $\tau_0 \ll t \ll \tau_e$: we skip the dynamics before the segmental relaxation time τ_0. Just beyond τ_0, the test chain does not feel the constraint of the obstacles. $\tau_e \cong \tau_0 N_e^2$ is the entanglement time indicating the onset of the entanglements. Thus, the initial relaxation will follow the Rouse dynamics as in a free space, since the effect of HI is not involved. We track the polymer dimension in the direction perpendicular to the initial stretching, $\langle R_{yy}^2 \rangle$. Starting from the full stretched configuration ($\langle R_{yy}^2 \rangle = 0$ at $t = 0$), the perpendicular size is a measure of structural fluctuation as a function of time. In comparison, the mean-squared (m.s.) polymer dimension parallel to the stretching direction is the sum of non-zero average and fluctuation terms, *i.e.*, $\langle R_{xx}^2 \rangle = \langle R_x \rangle^2 + \langle \delta R_{xx}^2 \rangle$. The average term is dominant at the retraction stage when $t \ll \tau_R$.

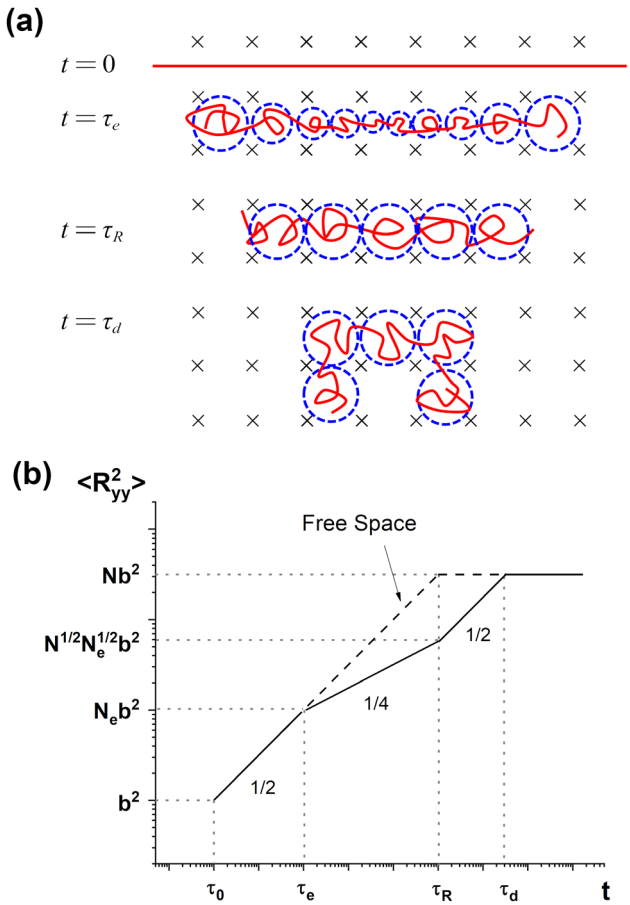


Fig. 1 (a) Theoretical illustration of the relaxation process of a fully stretched polymer chain in a fixed network of mesh size $a \cong N_e^{1/2}b$ at (i) entanglement time τ_e, (ii) Rouse time τ_R, and (iii) disentanglement time τ_d. (b) Summary of the structural recovery along the direction perpendicular to the stretch direction based on the classic reptation theory (solid line), in comparison to an unconstraint chain relaxing in free space (dashed line).

In the Rouse model, a strand of size $\xi \cong gb^2$ containing g segments that can relax by a given time t should satisfy $\tau_0 g^2 \cong t$, which means $g \cong (t/\tau_0)^{1/2}$. Thus,

$$\langle R_{yy}^2 \rangle \cong (t/\tau_0)^{1/2} b^2, \quad t \ll \tau_e \tag{1}$$

It must be noted that the relaxation rate varies along the chain's contour. The scaling expression of eqn (1) is valid for the strand at the chain's ends, but not for the middle strand without free ends. This is because the relaxed strand causes tension to the unrelaxed strand. The magnitude of the tension is inversely proportional to the relaxed strand size: $f_t \cong k_BT/\xi_t$, based on the definition of a tension blob.[2] Here, the tension blob size ξ_t is the relaxed strand size. Thus, eqn (1) should better align with the perpendicular component of m.s. end-to-end distance which represents the maximum structural fluctuation along the chain, rather than the radius of gyration which is a value smeared along the polymer's contour.

(ii) $\tau_e \ll t \ll \tau_R$: the test chain starts feeling the network constraint from the entanglement time τ_e. Due to the different relaxation rates along the chain's contour, τ_e should

This journal is © The Royal Society of Chemistry 2026

correspond to the time scale at which the chain ends begin to feel the network, while the internal segments remain unconstrained. For the terminal strand, the fluctuation along the perpendicular direction is significantly retarded. In contrast, the motion along the chains contour remains unaltered, and thus, it is the preferred pathway of relaxation. During this process, the PP, the shorted path connecting the chain ends remains a straight line, and thus, no entanglement is created in the internal strand. Meanwhile, the contour length of PP is significantly reduced with time. The fluctuation parallel to the initial stretching is still Rouse like: $\langle R_{\parallel}{}^2\rangle \cong (t/\tau_0)^{1/2}b^2$. The motion along the perpendicular direction is limited to the network strand size: $\langle R_{\perp}{}^2\rangle \cong a^2$. The global structural recovery is the average fluctuation:

$$\langle R_{yy}{}^2\rangle \cong \sqrt{\langle R_{\parallel}{}^2\rangle\langle R_{\perp}{}^2\rangle} \cong (t/\tau_0)^{1/4}N_e{}^{1/2}b^2, \quad \tau_e \ll t \ll \tau_R \quad (2)$$

The (1/4) power-law dependence with time in eqn (2) compared to the 1/2 power-law exponent in free space shows that structural recovery of the test chain is significantly hindered by the topological constraint of the network.

(iii) $\tau_R \ll t \ll \tau_d$: the contour length PP reaches its equilibrium value $L_{PP0} \cong (N/N_e)a \cong Za$ by the Rouse time τ_R. After that, there is no advantage for the end strand to retract along the PP and thus it starts exploring the space in an isotropic manner, leading to the reorientation of the PP and creates entanglement with the network. The entire chain thus exhibits reptation motion. It is noteworthy that in the plane normal to the initial stretching, the motion of the end-to-end vector remains Rouse-like, because there is no constraint for the end strand. But it takes τ_R for each step to occur and the corresponding step length is the fluctuation size at τ_R. That means:

$$\begin{aligned}\langle R_{yy}{}^2\rangle &\cong (t/\tau_R)^{1/2}\langle R_{yy}{}^2(\tau_R)\rangle \\ &\cong (t/\tau_0)^{1/2}N^{-1/2}N_e{}^{1/2}b^2, \quad \tau_R \ll t \ll \tau_d\end{aligned} \quad (3)$$

The dynamics in networks can also be affected by the effect of contour length fluctuation (CLF) when the entanglement number is not large. The fluctuation of PP contour length increases as a Rouse process $\delta L_{PP}{}^2 \equiv \langle L_{PP}{}^2\rangle - \langle L_{PP}\rangle^2 \cong (t/\tau_e)^{1/2}a^2$ when $\tau_e \ll t \ll \tau_R$, and reaches the equilibrium value $\delta L_{PP}/\langle L_{PP}\rangle \sim Z^{-1/2}$ when $t \gg \tau_R$. Compared to the expression without CLF, the modified term can be written as:

$$\frac{\langle R_{yy}{}^2\rangle_{CLF}}{\langle R_{yy}{}^2\rangle} \cong \begin{cases} 1+\mu Z^{-1/2}(t/\tau_R)^{1/2} & \tau_e \ll t \ll \tau_R \\ 1+\mu Z^{-1/2}, & t \gg \tau_R \end{cases} \quad (4)$$

where μ is a numerical factor in the order of unity.[2] Thus, the effect of CLF can cause a faster increase of $\langle R_{yy}{}^2\rangle$ in the regime of $\tau_e \ll t \ll \tau_R$, but only introduces a shift factor to $\langle R_{yy}{}^2\rangle$ without changing its time dependence when $t \gg \tau_R$.

The theoretical predictions on structural recovery are summarized in Fig. 1(b), in comparison to the unconstraint relaxation in free space.

The above theoretical picture was originally proposed to explain segmental relaxation under equilibrium, and the corresponding power-law regimes can also be identified in the m.s. segmental displacement: $g_1(t) \equiv \langle[\boldsymbol{r}_i(t_0+t) - \boldsymbol{r}_i(t_0)]^2\rangle$. Although the two scenarios, end-to-end vector relaxation from a fully stretched state and segmental relaxation under equilibrium, are considered equivalent in the sense of a scaling argument, it must be emphasized that they are intrinsically different from each other. A fully stretched configuration represents a non-equilibrium state well beyond the linear deformation regime and thus its relaxation involves non-equilibrium dynamics. The above theoretical explanation based on the classic reptation theory incorporates the quasi-equilibrium assumption. Its validity should be limited to the overdamped regime, which is usually assumed in polymer liquids. The main point is that the characteristic time scales, including τ_e, τ_R, and τ_d, obtained from equilibrium dynamics and reentanglement dynamics are not necessarily identical in their absolute values. Thus, we need to focus on their scaling dependences on chain length and entanglement length to distinguish the role of different mechanisms.

II.2 Reentanglement dynamics of a highly stretched polymer melt

We now turn to the reentanglement dynamics of polymer melts with equally stretched chains. In this case, the topological constraints come from the chains surrounding a test chain. Thus, the effective ''network constraint'' is evolving through time and should be redefined based on the stage of relaxation. We consider a monodispersed polymer melt of linear chains with $N \gg N_e$. At $t = 0$, all polymer chains in the melt are highly stretched, as shown in Fig. 2(a) ($t = 0$). Such an initial configuration is typically obtained after imposing a uniaxial extensional flow on the melt with a strain rate much larger than $1/\tau_R$. We assume the overlap number is very low in the level of the chain and there are nearly no topological constraints between the chains. In the other words, all the PPs in the melt are straight lines without kinks.

We propose the following model to understand the recovery of the stretched polymer melts, as illustrated in Fig. 2(a).

(i) $t \ll \tau_{je}$: because the polymer melt is fully unentangled at $t = 0$ based on our assumption, the initial relaxation of the melt should follow the unentangled dynamics. We define τ_{je} as the ''just-entangled'' time from which topological constraint between polymers is onset. Then, following the classic picture for the unentangled melt dynamics, the structure will exhibit a Rouse-like behavior:

$$\langle R_{yy}{}^2\rangle \cong (t/\tau_0)^{1/2}b^2, \quad t \ll \tau_{je} \quad (5)$$

Although the Rouse-like motion for unentangled melt dynamics is widely recognized, abundant evidence indicates that this model is insufficient to describe the true dynamics of an unentangled melt under strong deformation,[31–35] even after accounting for finite extensibility effect. The deviations from the Rouse model due to multi-chain interactions can be

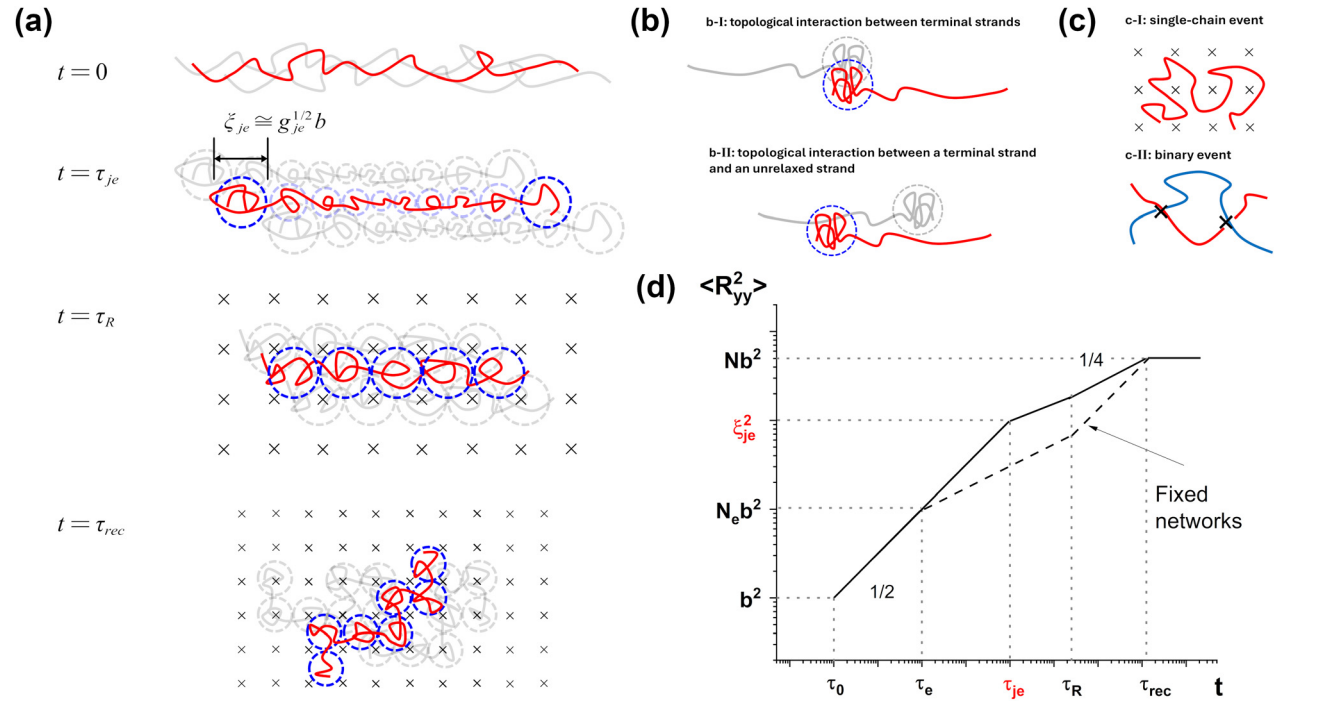


Fig. 2 (a) Theoretical illustration of the relaxation process of a test chain in a fully stretched polymer melt at different time scales. τ_{je} is defined as the "just-entangled" time from which the strands with free ends start feeling entanglement effect. The corresponding length scale is the "just-entangled" strand size ξ_{je}. τ_{rec} is the time scale at which the polymer equilibrium structure is fully recovered. (b) Comparison of topological interactions of a terminal strand with another terminal strand (case b-I) and with an unrelaxed strand (case b-II). This work assumes that entanglements are first created in case b-I when their overlap number exceeds a critical value. (c) Relationship between the number of entanglements per chain and the perpendicular size in a single-chain event (case c-I), where obstacles are preset in space, and in a binary event (case c-II), where entanglements in a melt rely on the binary contact of different chains. In the single-chain event case, the number of new entanglements relies on the range of space explored by a single polymer. In the case of binary events, the recovery of entanglements depends on the increased overlapping level between neighboring chains. (d) Summary of the structural recovery of a highly stretched melt along the perpendicular direction (solid line), in comparison to the relaxation in the fixed networks (dashed line).

attributed to two major effects from the current knowledge: correlation hole effect,[36,37] and hydrodynamic interaction.[38–40] The former effect accounts for local density fluctuation. Whereas the effect of HI in a melt, which was considered not long ago,[38–40] is more relevant to the large-scale configuration. Which factor is dominant and how the dynamic modes deviate from the Rouse model during relaxation remain under debate. Despite the complexity, our follow-up discussion on topological interaction is based on a structural analysis. The modification of the dynamic modes in the unentangled regime will not alter our explanation of the reentanglement process. Here, we keep the form of eqn (5) for this regime.

(ii) $\tau_{je} \ll t \ll \tau_R$: with the recovery of polymer structure, a test chain starts feeling the effect of entanglement from its neighboring chains. Then, the central question is, from which time and length scales topological interaction is onset? First, we recall that in a free space, relaxation of a stretched chain is not homogeneous along the polymer's contour. The strand close to the chain ends can relax faster than those in the middle. It also means that, in the melt, the magnitudes of overlapping between strands are different along the chain's contour. Particularly, the largest blobs representing the terminal strands should have the maximum overlap number. Then, we must consider the two different cases as drawn in Fig. 2(b). That is, how is a terminal strand that has already been relaxed, restricted by another terminal strand, and how this effect varies in the case of an unrelaxed strand? Here, we conjecture that the topological interaction between the relaxed strands in case b-I of Fig. 2(b) is more effective than that in case b-II. This hypothesis is partly inspired by the studies of non-concatenated ring polymer melts,[41–44] whose relaxation moduli do not exhibit an elastic entanglement plateau. The fractal loopy globules model proposed by Ge *et al.*[41] suggests a picture where the strands with no free ends will organize themselves in such a way that their overlap number at all length scales is always below criterion of entanglement onset. We extend this idea by considering the contact in case b-II of Fig. 2(b) will not lead to entanglement effect as the unrelaxed strand will avoid being entangled with the relaxed one. Based on this conjecture, we can proceed with the prediction of reentanglement dynamics of melts as follows.

We can consider the extreme case that at the onset of topological interaction, entanglements only occur between the relaxed terminal strands of the polymer chains (case b-I of Fig. 2(b)). We then define a "just-entangled strand" whose size is $\xi_{je} \cong g_{je}^{1/2} b$, where g_{je} is the number of segments in this

 This journal is © The Royal Society of Chemistry 2026

strand. It represents the minimum strand size that can be entangled with each other in the melt. We assume these strands are homogeneously dispersed. Then, we refer to the Lin–Nolanddi ansatz[27,28] which states that polymers become entangled when the overlapping between the coils reach a critical value (around 20). Using this criterion, we define the just-entangled strand from the overlap number $\mathcal{O}$:

$$\mathcal{O} = \frac{a^3\rho}{N_e} = \frac{2g_{je}}{N}\frac{{\xi_{je}}^3\rho}{g_{je}} \tag{6}$$

where ρ is the density of segments in the melt. The first equivalence of eqn (6) defines $\mathcal{O}$ from equilibrium dynamics. In contrast, there is an extra factor of $2g_{je}/N$ for the reentanglement dynamics, because except the segments in the just-entangled strands close to the chain extremities, the fluctuation range of other segments are so weak that they cannot effectively entangle with each other or with a just-entangled strand. From eqn (6), it is easy to derive:

$$g_{je} \cong N^{2/3}{N_e}^{1/3} \tag{7}$$

$$\xi_{je} \cong N^{1/3}{N_e}^{1/6}b \tag{8}$$

The just-entangled strand size ξ_{je} is thus an effective tube diameter at the onset of topological interaction. The main feature of ξ_{je} is that it is larger than the equilibrium tube diameter and it increases with the chain, since $\xi_{je}/a \cong Z^{1/3}$. The main argument is that longer chains have smaller density of terminal strands (twice of chain density), and thus, it requires more time to reach the overlap criterion. It must be noted that the derivation of the just-entangled strand only relies on polymer structure, regardless of the dynamics feature before the onset of topological interaction.

The corresponding just-entangled time is:

$$\tau_{je} \cong \tau_0{g_{je}}^2 \cong \tau_0 N^{4/3}{N_e}^{2/3} \tag{9}$$

Thus, the just-entangled time lies between the entanglement time and the Rouse time: $\tau_e \ll \tau_{je} \ll \tau_R$. That means, in the recovery of an entangled melt, the unentangled regime is much broader than expected from equilibrium dynamics ($t \ll \tau_e$) and relies on the chain length N. The identification of the just-entangled strand highlights the difference between equilibrium dynamics and reentanglement dynamics of a fully stretched polymer melt. Under equilibrium, there is no direct implication of the just entangled time τ_{je}.

In the regime of $\tau_{je} \ll t \ll \tau_R$, the polymer dynamics will be similar to the case of fixed networks when $\tau_e \ll t \ll \tau_R$. At this stage, the terminal strand still prefers retracting along the contour without significant increase for its size along the perpendicular direction. When we ignore the change of the effective confinement length, we have

$$\begin{aligned}\langle {R_{yy}}^2\rangle &\cong (t/\tau_0)^{1/4}{g_{je}}^{1/2}b^2 \\ &\cong (t/\tau_0)^{1/4}N^{1/3}{N_e}^{1/6}b^2, \quad \tau_{je} \ll t \ll \tau_R\end{aligned} \tag{10}$$

The expression in the first line of eqn (10) is the same as eqn (2) for relaxation in fixed networks, but the equilibrium entanglement length N_e is replaced by the just-entangled strand length g_{je}.

(iii) $\tau_R \ll t \ll \tau_{rec}$: τ_{rec} is defined as the full recovery time. After the Rouse time τ_R, PP starts reorienting like in fixed networks. The difference is that the entanglement network is densified with the recovery of polymer structure. To describe this process, we propose the following self-consistent model for the reentanglement process at the reorientation stage. The assumption is to consider the effective number of entanglements per chain relative to the equilibrium value as a power-law function of the relative perpendicular size $Z'/Z = f(\langle {R_{yy}}^2\rangle/Nb^2)$. Then, the question is what should be the exponent value? If the obstacles are preset in space as discussed in the last section and illustrated in case c-I of Fig. 2(c), the entanglement state of a polymer chain relies on its own configuration. It is natural to use the relation $Z'a^2 \cong \langle {R_{yy}}^2\rangle$. We call this situation a single-chain event.

However, this is not the case in a melt, where the obstacles are not preset. Here, we recall that the creation of entanglements in a melt relies on the binary contact between two different chains, which we call a binary event (case c-II). The idea of binary contact can trace back to de Gennes,[45] and is extended in many other cases like the CR in binary blends of entangled polymers.[46] In the present context, the formation of new entanglements requires two chains to inter-diffuse into the same overlap region. Consequently, the recovery of entanglements depends not only on the overlap recovery of a single chain but also on that of its neighboring chains. If the perpendicular dimension of each chain recovers as $\langle {R_{yy}}^2\rangle \sim t^a$, then the probability that two chains simultaneously occupy the same overlap region is proportional to the product of their individual overlap recoveries, giving $Z' \sim t^{2a}$. In other words, the entanglement recovery scales with the square of the overlap recovery because a binary contact can only be established when both chains have expanded sufficiently to overlap with each other. The entanglement recovery due to binary event is thus expressed as the following, compared to single-chain event:

$$\frac{Z'}{Z} \cong \begin{cases} \langle {R_{yy}}^2\rangle/Nb^2 & \text{single} \\ \left(\langle {R_{yy}}^2\rangle/Nb^2\right)^2, & \text{binary} \end{cases} \tag{11}$$

Then, we can modify the expression of eqn (3) for the regime $\tau_R \ll t \ll \tau_d$ in networks, which predicts a second Rouse-like behavior:

$$\langle {R_{yy}}^2\rangle \cong (t/\tau_0)^{1/2}Z'^{-1/2}b^2 \tag{12}$$

Because the instant entanglement number Z' is a function of $\langle {R_{yy}}^2\rangle$, eqn (12) is a self-consistent expression for the perpendicular size $\langle {R_{yy}}^2\rangle$. It suggests the relation:

$$\langle {R_{yy}}^2\rangle \cong \begin{cases} (t/\tau_0)^{1/3}{N_e}^{1/3}b^2 & \text{single} \\ (t/\tau_0)^{1/4}N^{1/4}{N_e}^{1/4}b^2, & \text{binary} \end{cases}, \quad \tau_R \ll t \ll \tau_{rec} \tag{13}$$

There is a mismatch between eqn (10) and eqn (13) at $t = \tau_R$, which can be smeared in the window of $\tau_{je} \ll t \ll \tau_R$ because

eqn (10) assumes a constant entanglement constraint. The assumption of binary events predicts a similar time dependence of $\langle R_{yy}{}^2\rangle$ as the relaxation in a network in the regime of $\tau_e \ll t \ll \tau_R$, and it is weaker than the prediction of single-chain event.

The full recovery time τ_{rec} is derived from eqn (13) by letting $\langle R_{yy}{}^2\rangle \cong Nb^2$. It says:

$$\tau_{rec} \cong \tau_0 N^3 N_e{}^{-1} \tag{14}$$

Within our assumption, the recovery time is consistent with the disentanglement time regardless of the assumption of single and binary events of entanglement. Thus, the reconstruction of entanglement of a melt may significantly modify the mode of relaxation, but it does not change the full relaxation time from the classic reptation theory. Such a claim is consistent with the interrupted flow experiments looking at the dependence on chain length of the full recovery time.[12] The recovery of entanglements of a melt, like the network case, mainly occurs in the reorientation stage from τ_R to τ_{rec}, in contrast to the rapid reentanglement dynamics at the Rouse time scale reported by previous simulation studies.[24,25]

The reentanglement dynamics from the above theoretical model are summarized in Fig. 2(b), in comparison with the case in fixed networks. We predict two main features of reentanglement dynamics of polymer melts: one is that the onset of topological interaction, which corresponds to the crossover from $\langle R_{yy}{}^2\rangle \sim t^{1/2}$ to $t^{1/4}$, can be delayed from the equilibrium entanglement time; the other is that $\langle R_{yy}{}^2\rangle$ should roughly exhibit two power-law regimes, in contrast to the three-power-law behavior in networks. The smeared regime $\tau_{je} \ll t \ll \tau_R$ should be too narrow to be effectively distinguished from the regime of $\tau_R \ll t \ll \tau_{rec}$.

II.3 Reentanglement dynamics of a stretched probe in a relaxed polymer matrix

Besides the above two scenarios, another interesting case to mention is the relaxation mechanism of a highly stretched polymer probe diluted in a matrix of relaxed polymer chains. The corresponding initial configuration can be obtained after a polydisperse sample is subjected to a flow whose rate is larger than the relaxation rate of the long chains but smaller than that of the short chains.[47] In this case, the relaxation of the long probe chains strongly relies on the CR process of the matrix chains. The equilibrium dynamics of the polydisperse samples have been investigated extensively.[48–50] However, their reentanglement dynamics have been rarely explored. Limited to the scope of this work and the difficulty of obtaining reliable simulations data, we leave this subject as a perspective of our future studies.

III Simulation methods

III.1 Polymer probe in a network

The above theoretical pictures on reentanglement dynamics are tested from MD simulations. We carry out simulations with LAMMPS.[51] To examine the reentanglement in networks, we prepare a 3D cubic grid fixed in the simulation box. The mesh size of the grid is d. The grid imposes topological constraint on the polymer probes. We assume the network is filled by an implicit Θ solvent for the polymer so that the molecular structures are consistent with the melts. Instead of simulating phantom chains, the intra-chain pairwise interaction is explicitly included, and the parameters are chosen so that the effects of attractive and repulsive parts of the pairwise potential happen to compensate each other. This approach is a more solid description of the Θ condition.[52]

Monomers interact with each other *via* the truncated Lennard-Jones (LJ) potential when their separation is smaller than a cutoff distance r_c:

$$U_{pair}(r) = 4\varepsilon[(\sigma/r)^{12} - (\sigma/r)^6], \quad r < r_c \tag{15}$$

where σ is the bead diameter, ε is the interaction strength. The potential is shifted to have a smoothed crossover at $r = r_c$. We use the LJ unit system in the rest discussions. The cutoff distance is set to $r_c = 2.50$ which means the pairwise potential includes an attractive part. The interaction strength is set to $\varepsilon = 0.30$. The finitely extensible nonlinear elastic (FENE) interaction potential is used for bonded beads:

$$U_{bond}(r) = -\frac{1}{2}kR_m{}^2 \ln\left(1 - r^2/R_m{}^2\right), \quad r < R_m \tag{16}$$

where $k = 30$ is the spring constant and $R_m = 1.50$ is the maximum stretch for a bond. Overlaid with the LJ potential between bonded beads, the equilibrium bond length is $l_b = 0.97$. Under these simulation parameters, the bond-vector correlation function of an isolated polymer chain decays with bond separation as a power law with an exponent of $(-3/2)$, indicating that the system is under the true Θ condition.[52]

We simulate both flexible (F) and semiflexible (SF) chains in this work to examine the potential effect of polymer's chemical structure, which has been raised as a non-negligible factor to consider.[24] The semiflexible chains are modelled by including an angle potential:

$$U_{angle}(\theta) = \kappa(1 - \cos\theta) \tag{17}$$

where θ is the angle between two subsequent bonds. The stiffness parameter is set to $\kappa = 2.10$ for semiflexible chains. In the main text, we will primarily present the data of semiflexible chains which have larger entanglement numbers. The data of flexible chains can be found in SI.

The grid is created from LJ particles of diameter σ_{grid}. They are placed along the grid lines and separated with the neighboring bead by a distance of σ_{grid}. Thus, each grid strand consists of d/σ_{grid} grid particles. These grid particles interact with monomers of polymer chains *via* the shifted LJ potential:

$$U_{LJ/exp}(r) = 4\varepsilon'\left[(\sigma/(r-\Delta))^{12} - (\sigma/(r-\Delta))^6\right], \quad r < r_c' + \Delta \tag{18}$$

 This journal is © The Royal Society of Chemistry 2026

where the shift factor is $\Delta = (\sigma_{grid} - 1.0)/2$. The interaction is set to be pure repulsive so that $r_c' = 2^{1/6}$. The interaction energy is $\varepsilon' = 1.0$.

The static and dynamic properties of a polymer chain in the space with fixed obstacles have been simulated by Baumgärtner and Muthukumar[53] many years ago. They found that the porosity of the space, or the volume fraction of the obstacles ϕ_{obs} is an important factor to consider. Not only the polymer's diffusivity but also the polymer size in the media significantly decreases with ϕ_{obs} when ϕ_{obs} is beyond a particular value. Indeed, when de Gennes[54] first proposed reptation motion in fixed networks, the obstacles should have no excluded volume and only impose topological constraint. There is no change in the configurational statistics of the polymers. Edwards and Muthukumar[55] then proposed a theory and explained that polymers in the presence of obstacles with finite excluded volume will collapse when $\phi_{obs} \gg N^{-1/2}$. This is in fact the condition when ϕ_{obs} becomes larger than the volume fraction of the monomers inside its own coil. We are aware of this transition in our simulations. We wish to focus on the effect of topological constraints in this work and thus ϕ_{obs} is kept low enough to promise clean reptation. In our simulation design, the total volume fraction of the grid particles is $\phi_{obs} = \pi(\sigma_{grid}/d)^2/2$. Thus, we use small grid particles to effectively reduce ϕ_{obs}. At the same time, to avoid topological violation and to promise a reasonable simulation time, σ_{grid} cannot be too small. We let $\sigma_{grid} = 0.5$, corresponding to a grid particle fraction $\phi_{obs} \approx 0.006$ when $d = 8.0$ (densest network to be examined in this work). In this case, the Edwards and Muthukumar[55] theory predicts polymers to collapse when chain length becomes larger than $N^* \cong {\phi_{obs}}^{-2} \approx 27\,778$. The largest chain length to be explored in our simulations is much smaller than this critical value. Thus, no structural change is expected from the theory. The absence of structural changes is also supported by our simulation data that polymer in a network always recovers to the same dimension as in free space, as will be shown later. Meanwhile, a chain crossing event between a polymer bond and the network strand of $\sigma_{grid} = 0.5$ has an energy barrier of around $200kT$, and thus, topological constraint will be well preserved.

Meanwhile, it must be noted that the Edwards–Muthukumar theory[55] is based on ideal chain model ignoring all intrachain pairwise interactions. In this work, we follow the modern theory of polymer's Θ condition[52] and model the chains with an intra-chain pairwise potential. The criteria of structural and dynamic transition with the space porosity must be significantly modified. We did not examine this transition systematically in this work, but it will be an interesting subject for our future studies.

The setups of simulations are summarized in Table 1. The motion of the polymer chain is integrated with the Langevin themostat, which means a friction force and a random force are imposed on the particles' motion. The reference monomeric friction coefficient is $\zeta_b = 1.0$. The intensity of the random force satisfies the fluctuation–dissipation theorem. The reduced temperature is $kT = 1.0$. The time step of simulations is $\delta t = 0.01$. We use a simulation box whose axis lengths satisfy $L_x \geq (N_b - 1)l_b$, and $L_y = L_z > R_0$, where R_0 is the equilibrium chain size. Fig. 3 presents simulation snapshots during the recovery process at different time scales. The snapshots in the network are compared to those in the free space. In these snapshots, 500 configurations are overlaid to show the extent of fluctuations. But there are no inter-chain interactions during the simulation.

Table 1 Simulation setups

		LJ parameters			
	Thermostat	ε	r_c	N_b/N_{chain}[a]	$L_x \times L_y$ (= L_z)
Network simulations	Langevin	0.30	2.50	20/500	50.0 × 50.0
				50/500	50.0 × 50.0
				100/500	100.0 × 100.0
				200/500	200.0 × 100.0
				500/500	500.0 × 100.0
				1000/500	1000.0 × 200.0
Melt simulations	DPD	1.0	$2^{1/6}$	20/500	22.7 × 22.7
				50/1000	50.0 × 34.3
				100/2000	100.0 × 48.5
				200/1000	100.0 × 48.5
				200/2000	200.0 × 48.5
				300/1000	150.0 × 48.5
				300/2000	300.0 × 48.5

[a] N_{chain} is the number of polymer chains per simulation. In a network simulation, multiple chains are simulated simultaneously in the same network, but the inter-chain interactions are turned off. Thus, the monomer density in a network simulation is $\rho = N_b/V$, in contrast to $\rho = N_b \times N_{chain}/V$ in a melt.

We examine chain lengths in the range of $5 \leq N_b \leq 1000$ in the networks of $d = 8.0$, 10.0, and 15.0. The entanglement length in the networks is uniquely determined by the network strand. The number of beads per entanglements strand N_{eb} in our simulation model is defined from the condition: $\langle dR_k^2 \rangle|_{k=N_{eb}} = d^2$, where $\langle dR_k^2 \rangle$ is the m.s. end-to-end distance of a strand containing k bonds under equilibrium. The corresponding values of N_{eb} (with error bars up to 1) are summarized in Table 2. The maximum entanglement number is around 30 (SF chain of $N_b = 1000$ in the network of $d = 10.0$). For some simulation parameters, the running time required to observe the full relaxation was too long. To improve computational efficiency, we adopted the time-friction superposition. The idea is to run the simulation with a smaller monomeric friction coefficient $\zeta_b' < \zeta_b$. Then a running time t' with a reduced friction should correspond to the timescale of $t = t'/\zeta_b'$ under the reference friction coefficient. The validity of time-friction superposition is discussed in Section A of SI.

III.2 Polymer melts

We also use the KG-type simulation model for polymer melts. The bonded and angle potential functions and the corresponding interaction parameters are the same as network simulations. But for pairwise potential, we set a shorter cutoff distance $r_c = 2^{1/6}$ and a unit energy parameter $\varepsilon = 1.0$, which means the monomers in the melts are purely repulsive. The main purpose for this change is to improve computation

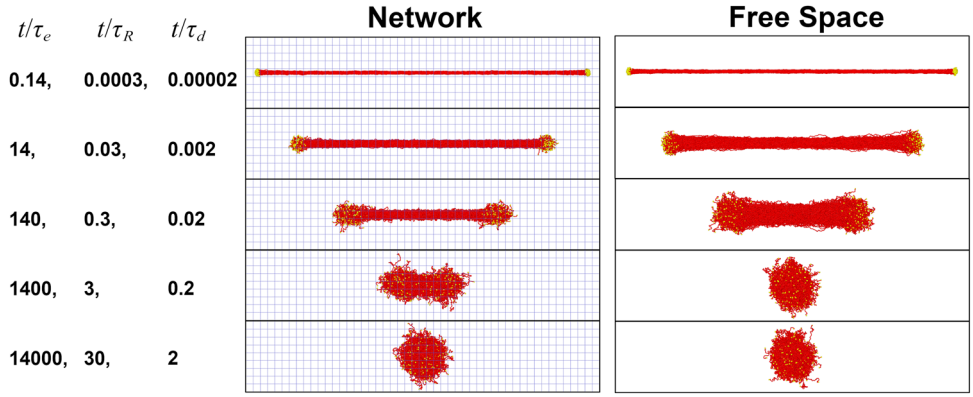


Fig. 3 Simulation snapshots for semiflexible chains of length N_b = 500 in the network of d = 10.0 (left) and in free space (right) at different time scales, visualized from OVITO.[56] In this figure, the centers of mass of 500 configurations are shifted to the center of the simulation box. Chain ends are marked as yellow beads.

Table 2 Entanglement lengths of simulation models

	Polymer type[a]	Entanglement length[b]	Number of beads per entanglement N_{eb}[c]
Network simulations	F	8.0	33
		10.0	50
		15.0	109
	SF	8.0	21
		10.0	32
		15.0	70
Melt simulations	F	10.9	57 (75)
	SF	8.5	23 (19)

[a] "F" for "flexible chains", and "SF" for "semiflexible chains". [b] Entanglement length means network mesh sizes d for network simulations and tube diameter $a \equiv \langle R_0^2\rangle/\langle L_{PP0}\rangle$ for melt simulations, where $\langle L_{PP0}\rangle$ is the average contour length of PP under equilibrium. [c] Number of beads per entanglement is defined as $\langle dR_k^2\rangle|_{k=N_{eb}} = d^2$ or a^2. Values in the brackets are those estimated from the empirical expressions by Svaneborg and Everaers,[58] which are also based on PPA.

efficiency without altering dynamic modes. It has been proved from several studies that the simulation models of melts with repulsive and attractive potentials exhibit very similar dynamic behaviors in their liquid state.[40,57] The simulations are performed under the NVT ensemble at the bead density ρ = 0.85. A dissipative particle dynamics (DPD) thermostat is used with a damping parameter γ = 1.0. In Section B of SI, we also compared the constant-volume simulation with the constant-pressure (NPT ensemble) simulation which allows free lateral contraction. The results are almost indistinguishable from each other.

Simulation setups and the entanglement lengths of the melt models are also summarized in Tables 1 and 2. In the melt simulations, we evaluate equilibrium tube diameter as:[9] $a \equiv \langle R_0^2\rangle/\langle L_{PP0}\rangle$, where $\langle R_0^2\rangle$ is the overall m.s. end-to-end distance and $\langle L_{PP0}\rangle$ is the average contour length of PP under equilibrium (details to be presented in a later section). The number of beads per entanglement N_{eb} is then defined from the condition $\langle dR_k^2\rangle|_{k=N_{eb}} = a^2$. The corresponding values are presented in Table 2, which are close to those from the empirical expressions by Svaneborg and Everaers.[58] We will discuss chain lengths up to N_b = 300, corresponding to 15 entanglements in the semiflexible systems.

To minimize finite-size effects while maintaining reasonable computational costs, we prepared two sets of systems with different simulation box sizes for the melts of N_b = 200 and 300, as shown in Table 1. In Section C of SI, we compare the corresponding simulation data and confirm that finite-size effects vanish beyond a certain time scale before full relaxation is reached. Therefore, in the simulation data presented below, we combine the short-time relaxation obtained from the larger simulation box with the long-time relaxation obtained from the smaller simulation box.

In this work, the initial configurations of melt simulations consisting of highly stretched chains are pre-equilibrated under tensile forces f_t to the chain ends parallel to the x-axis and pointing in opposite directions. This avoids performing non-equilibrium simulations of applying flows and the initial configurations are easier to control. Meanwhile, we generate initial configurations with $\langle R_{yy}^2\rangle$ = 0 and the end beads are only allowed to move along the x-axis in the preparation stage. The objective of letting $\langle R_{yy}^2\rangle$ = 0 is to characterize the initial stage of relaxation to identify the onset of topological interaction. A disentangled state is also promised when pre-equilibrating in this way. By applying a tension of $f_t l_b/kT$ = 10, we obtain highly stretched initial configurations whose bond order parameters are $s_0 \approx 0.90$, where $s \equiv \langle l_{bx}^2 - l_{by}^2\rangle/l_b^2$, and $l_{b\alpha}$ is the component of a bond vector along one axis. By reducing the applied tension, we also prepared less stretched but still disentangled configurations with $s_0 \approx 0.20$ and 0.50. After pre-equilibrium, the chain ends are released and the polymers in the melts start recovering. The simulation snapshots of the melt relaxation are shown in Fig. 4.

IV Result and discussion

IV.1 Simulation data of structural recovery

Equilibrium dynamics are examined first before investigating reentanglement dynamics in terms of the m.s. monomeric displacement function and center-of-mass (c.m.) diffusion

 This journal is © The Royal Society of Chemistry 2026

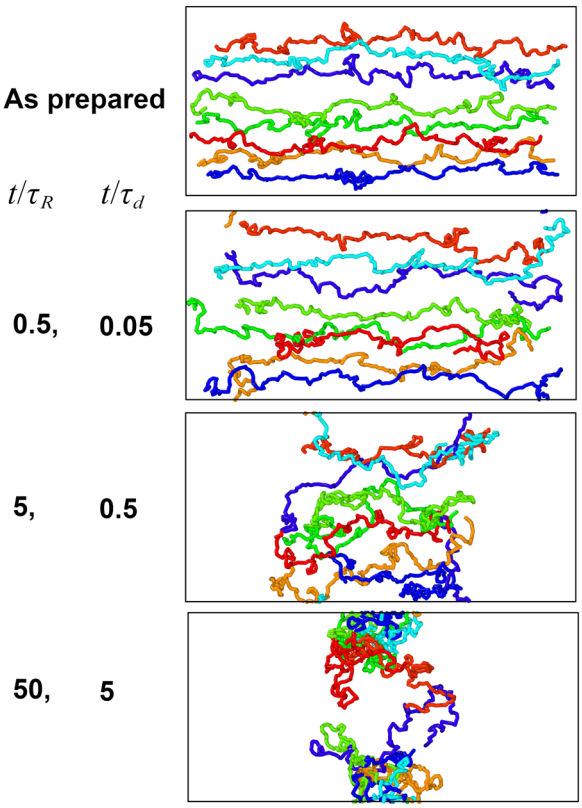


Fig. 4 Simulation snapshots for the recovery of the polymer melt consisting of semiflexible chains with N_b = 200 and s_0 = 0.20.

constant. The corresponding results are presented in Section D of SI. From a quantitative analysis, we confirm that the reptation theory well explains the dynamics of a test chain in networks and in their monodisperse melts from our simulations. The main message is that, under equilibrium, the test-chain dynamics in networks and entangled melts can hardly be distinguished from each other. However, this level of similarity contrasts with their reentanglement dynamics to be discussed in the following.

Then we turn to the structural recovery of polymers structures starting from highly stretched configurations. The evolution of m.s. end-to-end distance along the perpendicular direction $\langle R_{yy}{}^2\rangle$ of a fully stretched polymer chain in networks of different mesh sizes is shown in Fig. 5(a) and (b). The results are compared to relaxation in a free space. In this figure, the simulation data before reaching steady state of a well entangled sample can be clearly classified into three power-law regimes as predicted by the classic reptation theory. A fully stretched chain in a free space exhibits a single power-law relaxation before the full structural recovery. Whereas in a network the chain's relaxation deviates from the free-space behavior from a time scale, which increases with the network mesh size d, showing the onset of topological interaction. This time scale is known as the entanglement time τ_e, which is independent of chain length but increases with the network strand length. When $t > \tau_e$, the recovery of perpendicular size slows down, but it remains independent of chain length until a second crossover time. After that, a second regime showing $\langle R_{yy}{}^2\rangle \sim t^{1/2}$ is observed. What is remarkable is the broadness of this regime, compared to the regime $\tau_{R0} \ll t \ll \tau_{d0}$ in the monomeric diffusion function $g_1(t)$. These qualitative features are well consistent with the theoretical prediction as shown in Fig. 1(b). We also examine the m.s. radius of gyrations, which exhibit qualitatively similar behavior, as shown in Section F of SI. However, their agreement with theory is less satisfactory than the end-to-end distances, highlighting the importance of focusing on the maximum fluctuation. Besides, the average end-to-end distances along the direction of initial orientation $\langle R_x\rangle$ are shown in Fig. 5(c). By plotting the normalized values $\langle R_x\rangle/L$ against t/τ_R, we prove that initial retraction of the chain well agrees with the Rouse time. Whereas topological interactions with the network retard the reorientation process when $t > \tau_R$, leading to a slow terminal relaxation.

Characteristic time scales are extracted from the structural data. We first fit the simulation data in the free space *via* the function: $\langle R_{yy}{}^2\rangle(t) = A[1 + (t/\tau_R)^{-\alpha}]^{-1/2/\alpha}$. A sharp crossover is assumed by letting α = 10. The relation $\tau_R \sim N_b{}^2$ is well confirmed from the best-fit values. The monomeric relaxation time is then defined as $\tau_0 \equiv \tau_R/N_b{}^2$ for the convenience of discussion. The corresponding values are 0.14 and 0.10 for semiflexible and flexible chains, respectively. These definitions of Rouse time and monomeric time are fixed throughout the discussions about network simulations.

For simulation data in networks, we fit the time-dependent perpendicular size $\langle R_{yy}{}^2\rangle$ from a continuous function that describes all power-law regimes:

$$\begin{aligned}\langle R_{yy}{}^2\rangle(t) &= A\left[1+\left(t/\tau_e^*\right)^{-\alpha}\right]^{-(m-n-k)/\alpha}\left[1+\left(t/\tau_R^*\right)^{-\alpha}\right]^{-(n-k)/\alpha} \\ &\times\left[1+\left(t/\tau_{rec}^*\right)^{-\alpha}\right]^{-k/\alpha}\end{aligned} \quad (19)$$

Here, the superscript "*" is used to represent the values from reentanglement dynamics. The parameters m, n, and k describe the exponent values in the regimes of $t \ll \tau_e^*$, $\tau_e^* \ll t \ll \tau_R^*$, and $\tau_R^* \ll t \ll \tau_{rec}^*$, respectively. The sharpness factor of α = 10 is used as well.

We examine our simulation data in two steps. The first step is to let the exponents (m, n, and k) and the characteristic times (τ_e^*, τ_R^*, and τ_{rec}^*) as free parameters. For the data of N_b = 1000 and d = 10.0 in Fig. 5(a), the best-fit exponents are m = 0.607 ± 0.042, n = 0.258 ± 0.003, and k = 0.497 ± 0.004, well consistent with the theoretical values (1/2, 1/4, and 1/2) as shown in Fig. 1(b).

Because involving too many free parameters in the fitting can cause ambiguities, our follow-up analysis of the time scales is to fit $\langle R_{yy}{}^2\rangle$ from eqn (19) while fixing m = 1/2, n = 1/4, and k = 1/2. The best-fit curves are shown Fig. 5(a) and (b), representing a nice description of the raw data. The entanglement times τ_e in different networks are summarized in Fig. S7 of SI. The results show that the entanglement times from our network simulations agree well with the theoretical expression $\tau_e \sim N_{eb}{}^2$.

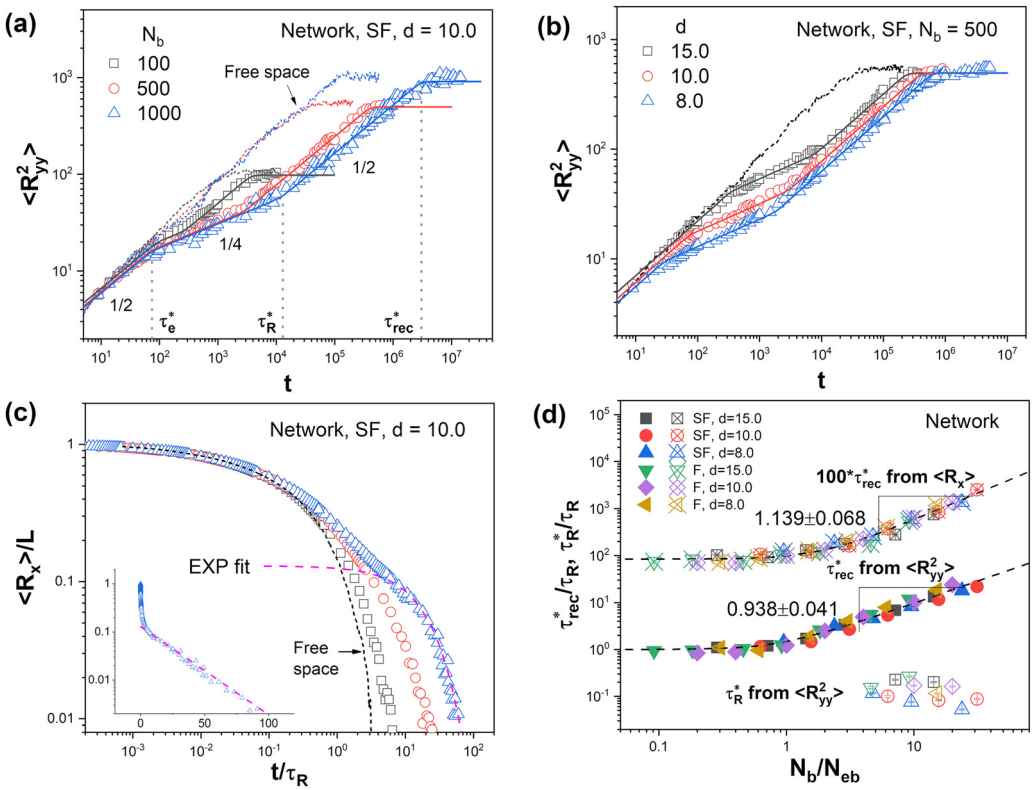


Fig. 5 Time evolution of perpendicular size $\langle R_{yy}{}^2\rangle$ in networks. (a) Polymers of different lengths in the same network of d = 10.0. (b) Polymer chain with N_b = 500 in different networks. The dotted lines in (a) and (b) are the data in free space. The solid lines are best fits from eqn (19) with m = 1/2, n = 1/4, and k = 1/2. In (a), the best-fit characteristic times, including the entanglement time τ_e^*, the Rouse time τ_R^*, and the recovery time τ_{rec}^* for N_b = 1000 are marked in the figure. (c) Average end-to-end distance along the direction of initial orientation normalized by the contour length $\langle R_x\rangle/L$, against the time normalized by the Rouse time t/τ_R, for different chains in the same network as in (a). The magenta dashed line is the single exponential function fit of the terminal regime. The inset showing a linear relation between log[$\langle R_x\rangle/L$] and t indicates the applicable range of exponential fit. (d) Summary of the recovery time τ_{rec}^* (solid scatters: fitting $\langle R_{yy}{}^2\rangle$ from eqn (19); crossed scatters: exponential fit of $\langle R_x\rangle$ and vertically shifted by two magnitudes) and the Rouse time τ_R^*. All values are normalized by the Rouse time τ_R defined from the dynamics in the free space and plotted against the number entanglements per chain (N_b/N_{eb}). The dashed lines in (d) are best-fit curves from a crossover function: $\tau_{rec}^*/\tau_R \cong \left[1+(\beta N_b/N_{eb})^2\right]^{-m/2}$, with the power-law exponents marked in the figure.

However, the numerical factors $\tau_e/\tau_0 N_{eb}{}^2$ is larger in equilibrium dynamics and in semiflexible chains.

The full recovery time τ_{rec}^* and the Rouse time τ_R^* by fitting the data of $\langle R_{yy}{}^2\rangle$ are presented in Fig. 5(d). All values are normalized by the Rouse time τ_R defined as the recovery time in the free space and plotted against the number entanglement per chain N_b/N_{eb}. We also estimate the recovery time from the single exponential fit of the average stretch along x-axis: $\langle R_x\rangle \sim \exp(-t/\tau_{rec}^*)$. Such an exponential fit is applicable for the terminal regime of $\langle R_x\rangle$, which behaves as a linear curve in the linear-log plot as the inset of Fig. 5(c). For τ_{rec}^* evaluated from either $\langle R_{yy}{}^2\rangle$ or $\langle R_x\rangle$, we confirm a good collapse of the data in this plot, regardless of chain length, network strand size, and chain chemistry. Using a similar method for c.m. diffusion constant, the τ_{rec}^* data are fitted from the function: $\tau_{rec}^*/\tau_R \cong \left[1+(\beta N_b/N_{eb})^2\right]^{-m/2}$. For τ_{rec}^* evaluated from $\langle R_{yy}{}^2\rangle$, the best-fit parameters are β = 1.131 ± 0.110 and m = 0.938 ± 0.042. For τ_{rec}^* from $\langle R_x\rangle$, the corresponding parameters are β = 0.543 ± 0.073 and m = 1.139 ± 0.068. In general, both groups of data are consistent with the theoretical prediction. The larger exponent value for τ_{rec}^* from $\langle R_x\rangle$ represents a better agreement with the reptation theory modified with CLF effect. For the Rouse times τ_R^* fitted from $\langle R_{yy}{}^2\rangle$, we found they are systematically smaller than the stretch-to-coil time in a free space and they do not collapse well like τ_{rec}^*. The ambiguity originates from the fact that τ_R^* becomes difficult to identify if the chains are not well entangled. But overall, the dependence on chain length $\tau_R^* \sim N_b{}^2$ is well confirmed. In summary, our simulation data proves that the classic reptation theory predicting a fast retraction followed by a slow reorientation process is quantitatively valid in explaining the reentanglement dynamics in networks.

We then investigate the time evolution of perpendicular size $\langle R_{yy}{}^2\rangle$ in entangled melts, starting from stretched and disentangled chains. The results are shown in Fig. 6(a) and (b), when the initial configurations have s_0 = 0.90 and 0.20, respectively. Terminal relaxation is reached for the longest chain N_b = 300, as confirmed from their isotropic polymer configuration by the end of the simulation. The change of $\langle R_{yy}{}^2\rangle$ in an entangled

 This journal is © The Royal Society of Chemistry 2026

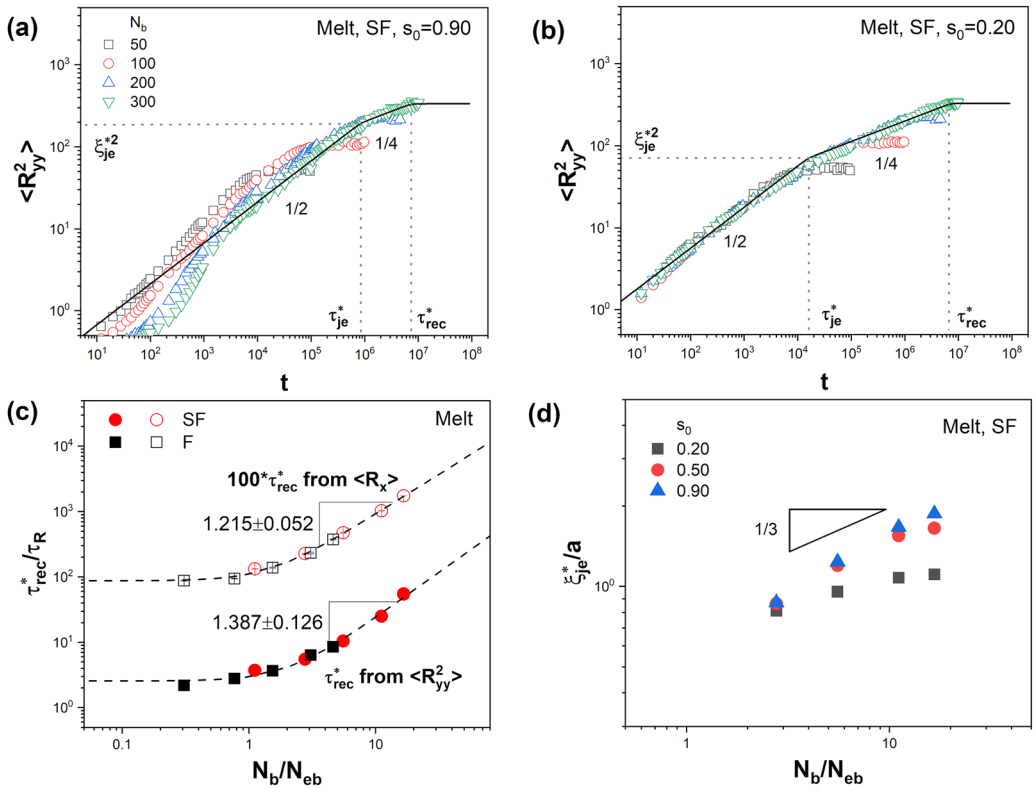


Fig. 6 Time evolution of perpendicular size $\langle R_{yy}{}^2 \rangle$ in entangled melts for semiflexible chains of $50 \leq N_b \leq 300$ when the initial configuration has (a) s_0 = 0.90 and (b) s_0 = 0.20. The solid lines are the best-fit curves from eqn (20) with m = 1/2 and n = 1/4. The best-fit values of the just-entangled time τ^*_{je} and the recovery time τ^*_{rec}, as well as the just-entangled length scale ξ^*_{je}, are marked in the figures. (c) Summary of the full recovery time τ^*_{rec} normalized by the Rouse time τ_R. (d) Summary of just-entangled size ξ^*_{je} normalized by the equilibrium tube diameter a.

melt is clearly distinguished from the structural recovery in a network as presented in Fig. 5. The classification into four regimes as predicted by the classic reptation theory and proved from our network simulations does not exist in a relaxing melt. Instead, the data before equilibrium can be roughly divided into two power-law regimes when $t > 10^3$ in $N_b \geq 200$. The second regime has smaller power-law exponent compared to the first one, indicating the effect of topological interaction. Although it is tempting to consider the second regime in Fig. 6(a) as a crossover to the plateau, a close examination of the data shows that this regime can persist for around one magnitude in the melt of N_b = 300, which can be considered as an indication of a different dynamic mode. Moreover, the second power-law regime is more distinguishable in Fig. 6(b) when we start relaxing from a less stretched configuration. Qualitatively, this two-power-law behavior of $\langle R_{yy}{}^2 \rangle$ is consistent with our theoretical prediction as summarized in Fig. 2(d). The main feature is that when a melt relaxes from a highly stretched state, the onset of entanglement effect should be postponed, and $\langle R_{yy}{}^2 \rangle$ will not exhibit a second Rouse-like behavior at the reorientation stage due to the creation of new obstacles in a self-consistent manner.

The regime corresponding to unentangled dynamics needs to be explained carefully. Fig. 6(a) shows that in this regime different chain lengths do not overlay with each other when s_0 = 0.90. If we start from a less stretched state as in Fig. 6(b), the unentangled regimes of different samples agree well. When $t < 10^3$, we found an unexpected fast recovery up to the length scale of $\langle R_{yy}{}^2 \rangle \approx 8$ (around 3 monomers) in Fig. 6(a). This regime is attributed to the reorganization of monomers' packing, as confirmed by monomer–monomer pairwise correlation functions shown in Fig. S11 of SI. When $t > 10^3$, the recovery of a longer melt is more delayed than the short ones. Such a phenomenon resembles a higher monomeric friction along the perpendicular direction, which has been reported by the current authors[35] from the nonlinear extensional rheology data of unentangled melts. We attribute this behavior to the memory effect. That is, when the chain retracts, it leaves a trace that cannot be instantly filled by the other chains.[59] This effect causes a local crowding that slows down the relaxation before the Rouse time.

We apply a quantitative method similar to that used for the network simulations to analyze the melt simulation data. We fit $\langle R_{yy}{}^2 \rangle$ from the following expression:

$$\langle R_{yy}{}^2 \rangle(t) = A\left[1 + \left(t/\tau^*_{je}\right)^{-\alpha}\right]^{-(m-n)/\alpha}\left[1 + \left(t/\tau^*_{rec}\right)^{-\alpha}\right]^{-n/\alpha} \quad (20)$$

We ignore the data before $t = 10^3$ for fitting that is influenced by finite-size effect. The exponent values are examined first. For

the data of N_b = 300, we find m = 0.560 ± 0.001, n = 0.285 ± 0.003 for s_0 = 0.90 and m = 0.437 ± 0.002, n = 0.287 ± 0.001 for s_0 = 0.20. Thus, in the second power-law regime, the melt simulation data agrees more closely with the self-consistent theoretical prediction assuming binary-contact entanglement creation, $\langle R_{yy}{}^2\rangle \sim t^{1/4}$, than with the single-chain event prediction $\langle R_{yy}{}^2\rangle \sim t^{1/3}$.

For the analysis of time and length scales, we fit the $\langle R_{yy}{}^2\rangle$ data while letting m = 1/2 and n = 1/4. The best-fit curve for the longest chain is shown in Fig. 6(a). Like Fig. 5(c) for network simulations, we also perform single exponential fit on the average end-to-end distance along direction of stretch to evaluate the terminal relaxation time of the melts: $\langle R_x\rangle \sim \exp\left(-t/\tau^*_{rec}\right)$. The data of recovery time normalized by the Rouse time τ^*_{rec}/τ_R are summarized in Fig. 6(c). In the melt, the Rouse time is defined as $\tau_R \equiv 10\tau_0 N_b{}^2$, where τ_0 is the monomeric time of the network simulations. The factor of 10 accounts for the higher monomeric friction coefficient as indicated by the c.m. diffusion constant in Fig. S6(b). The data showing an approximately linear relationship between τ^*_{rec}/τ_R and the entanglement number per chain N_b/N_{eb} proves that the terminal relaxation is still governed by the reptation dynamics, modified with the effect of CLF. This result is consistent with our theoretical prediction in Section II.2 and the experimental data from interrupted shear measurements.

The other quantity of interest is the length scale showing the onset of entanglement effect, which is considered as the just-entangled strand length rather than the equilibrium tube diameter in our theory. In the simulation data, the just-entangled strand length is defined as the crossover points where the time-dependence of $\langle R_{yy}{}^2\rangle$ changes from $t^{1/2}$ to $t^{1/4}$: $\xi^{*2}_{je} \equiv \langle R_{yy}{}^2\rangle|_{t=\tau^*_{je}}$. We consider that the horizontal shift of the unentangled regime affects the time scale of entanglement onset, but not the length scale. The values of ξ^*_{je} normalized by the equilibrium tube diameter against the entanglement number are shown in Fig. 6(d). The results show that the onset of topological interaction occurs at a larger length scale with the increase of chain length when the initial configuration is highly stretched. The dependence of ξ^*_{je}/a on entanglement number for s_0 = 0.90 is close to the theoretical prediction ($\xi^*_{je}/a \cong Z^{1/3}$ in eqn (8)) (we do not fit the exponent value because there are not enough data point), which is derived by assuming only effective topological interaction between relaxed terminal strands and the validity overlapping criterion. In comparison, when the initial configuration has s_0 = 0.20, but remains fully disentangled, the onset of entanglement effect becomes much insensitive to the chain length, like the case of networks. It shows that if the strand can partially relax initially, the two cases as discussed in Fig. 2(b) about the topological interaction between terminal strands and the middle strands, will be less distinguishable from each other.

In the theoretical section of this work, a major new consideration for the reentanglement dynamics is that the recovery of polymer structure is inhomogeneous along the chain's contour. The terminal strands with free ends will relax prior to those in the internal domain. To demonstrate this point, we present the distribution of bond order parameters at different time scales in Fig. 7. In this figure, we compare the network and melt simulations when they have a similar number of entanglements ($N_b/N_{eb} \approx 15$) at the range of $0.001 \le t/\tau_R \le 10$. For the network simulation in Fig. 7(a), the inhomogeneous relaxation with smaller ordering near the chain ends persists in the entire regime of time. By the moment of $t \approx \tau_R$, all bonds become close to the isotropic state. For the melt simulation in Fig. 7(b), although smaller ordering of bonds near chain ends is also identified when $t \ll \tau_R$, the overall distribution of s_i is more homogeneous than the that in the network simulation. Enhanced inhomogeneity is observed when $t/\tau_R \gg 0.1$. To prove whether new entanglements are built from chain ends in melts as expected by the theory, a direct analysis from PPA is necessary, which is to be discussed in the follow-up section.

In summary, in this section we prove the qualitative difference of the reentanglement dynamics between a probe chain in networks and an entangled polymer melt as predicted by our theoretical picture in Section II. The former case quantitatively agrees with the classic reptation theory. Whereas in the latter

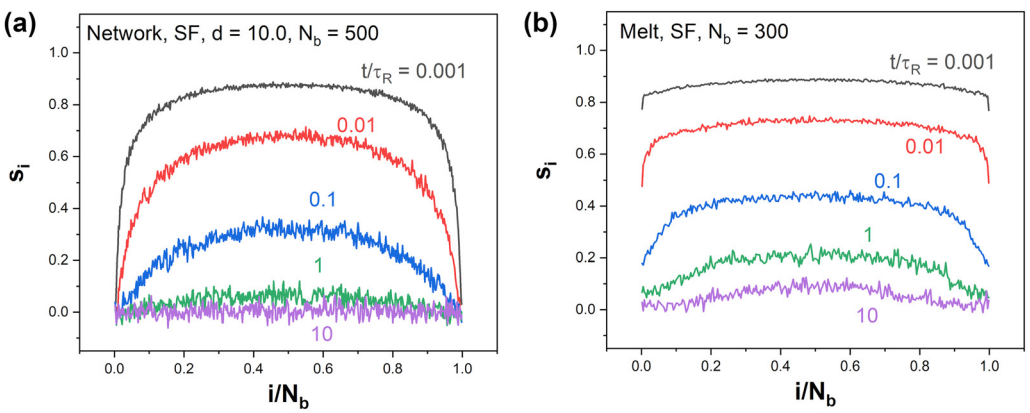


Fig. 7 Distribution of bond order parameters along the chain's contour $s_i \equiv \langle l_{bix}{}^2 - l_{biy}{}^2\rangle/l_{bi}{}^2$, where l_{bix} is the component of ith bond vector, at different times relative to the Rouse time τ_R in (a) network and (b) melt simulations with similar number of entanglements per chain.

 This journal is © The Royal Society of Chemistry 2026

case we need to consider the delayed onset of topological interaction and the increase of entanglement in a self-consistent manner. We also found that the relaxation of the melt before the onset of entanglement, which is thought to be Rouse-like, exhibits more complicated behavior than expected. The inhomogeneous structural recovery along the chain's contour, which is an important consideration of our theory, is well confirmed. However, the comparison between network and melt simulations suggests a direct check of entanglement properties is required.

IV.2 Primitive path analysis

Following the structural recovery of the original chains, the properties of primitive paths at different time scales during the reentanglement process are examined in this section. A primitive path is the shortest path connecting the two chain ends without violating the topological constraints. By analyzing the statistical properties and configurations of PPs, we can determine the entanglement state of the sample.[9] Thus, PPA provides significant insights into the relaxation pathway of a disentangled sample in addition to the original chain structure.

There are two major methods of performing PPA with MD simulation data. One is to quench the system while (i) fixing the motion of chain ends; (ii) turning off intrachain pairwise potential so that the contour length of the chain will shrink, and (iii) maintaining the interchain pairwise potential so that topological constraint is preserved.[9] The other method is to perform a pure geometric analysis, using the so-called Z1+ toolkit.[60] Although the Z1+ toolkit is generally more efficient than the quenching method, it is not applicable to our network simulations. Since it has been proved that the outcomes of the two methods have no significant difference,[60] we use the more adaptable quenching method throughout this work. Fig. 8 presents the simulation snapshots before and after PPA in a network and a melt.

We first focus on the average contour lengths of PPs, $\langle L_{PP}\rangle$. Fig. 9 plots their variation with time during the reentanglement process. We normalize $\langle L_{PP}\rangle$ by the contour lengths of the original chain L and plot them against the time normalized by the Rouse time. The results of network simulations are shown in Fig. 9(a). This figure confirms that Rouse time τ_R is the characteristic retraction time of PP contour length from the initial configuration (a fully stretch state, *i.e.*, $\langle L_{PP}\rangle/L = 1$) to the steady state. Moreover, a smaller network mesh size d results in a higher equilibrium retraction factor (for semiflexible chains, $\langle L_{PP0}\rangle/L \approx 0.10$ and 0.17 when $d = 15.0$ and 8.0, respectively). It means the level of bond length shrinkage during the generation of PP is lower, because the chain feels more topological constraints. In terms of the chain's chemistry, semiflexible chains have larger equilibrium value of $\langle L_{PP}\rangle/L$ than flexible chains in the same network. Semiflexible chains span a wider range, and thus, experience more effective entanglements. The melt simulations in Fig. 9(b) exhibit very similar behavior to network simulations. The relative retractions of contour lengths for different chain lengths of the same chemistry are well superposed when normalized by Rouse time. In terms of the equilibrium contour length, the retraction factor $\langle L_{PP0}\rangle/L$ in a melt of flexible chains is much smaller than that with semiflexible chains ($\langle L_{PP0}\rangle/L \approx 0.16$ compared to 0.40). This is a combined effect from the change of chain chemistry and tube diameter.

We further analyze the average number of entanglements during the reentanglement process. We check this property from the classic definition of entanglement number that treats PP as a Kuhn chain: $Z_{PP} \equiv \langle L_{PP}\rangle^2/\langle R^2\rangle$. $Z_{PP} = 1$ means that the PP is a straight line without kinks. The corresponding results of network and melt simulations are shown in Fig. 10. For the equilibrium values of Z_{PP} in networks, we find them much smaller than the entanglement number when the entanglement length is defined from the condition $\langle dR_k^2\rangle|_{k=N_{eb}} = d^2$, although the latter definition is well consistent with the equilibrium c.m. diffusion constant (Fig. S6(a)) and structural recovery time (Fig. 5(d)). For example, the chain of $N_b = 500$ in the network of $d = 10.0$ has $N_b/N_{eb} \approx 15$, but PPA shows that $Z_{PP} \approx 2.67$. Such a significant contrast has not been reported before. In comparison, PPA gives a more consistent estimation of entanglement property in polymer melts. The reasoning could be related to the difference between "pairwise" and "collective" entanglements.[61]

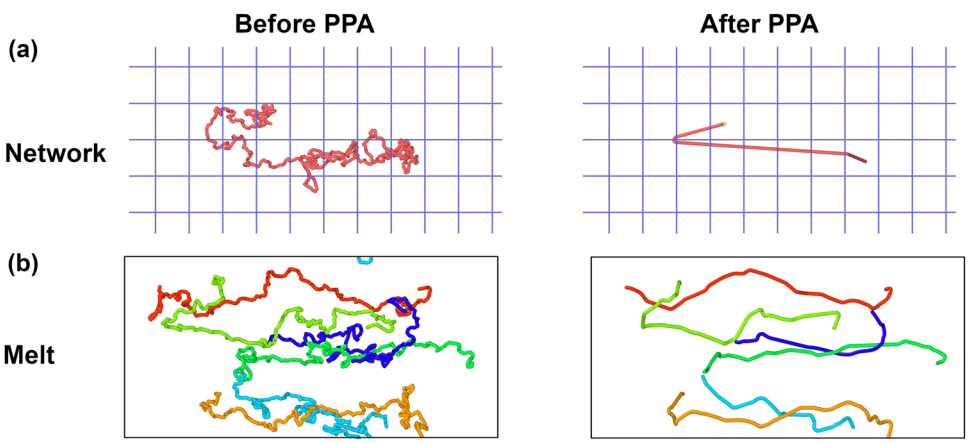


Fig. 8 Simulation snapshots before and after PPA in (a) a network and (b) a melt.

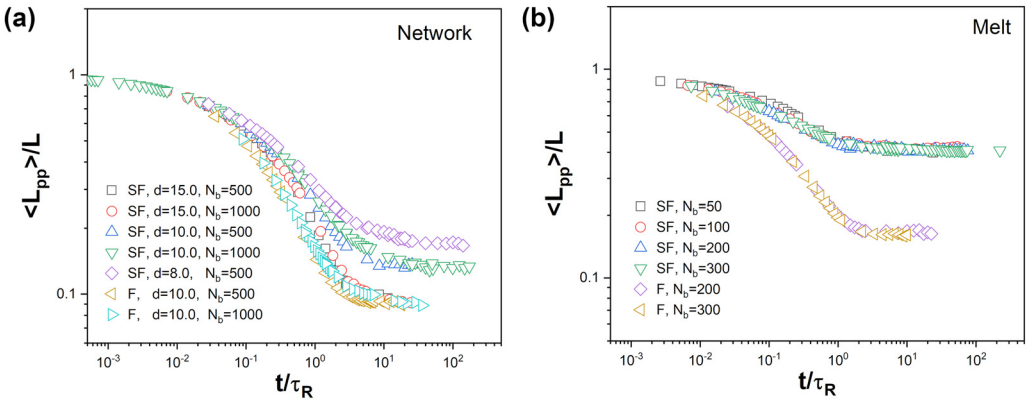


Fig. 9 Average contour length of PP normalized by the contour length of the original chain $\langle L_{PP}\rangle/L$ as a function of time normalized by Rouse time t/τ_R in (a) networks and (b) melts, for flexible (F) and semiflexible (SF) chains.

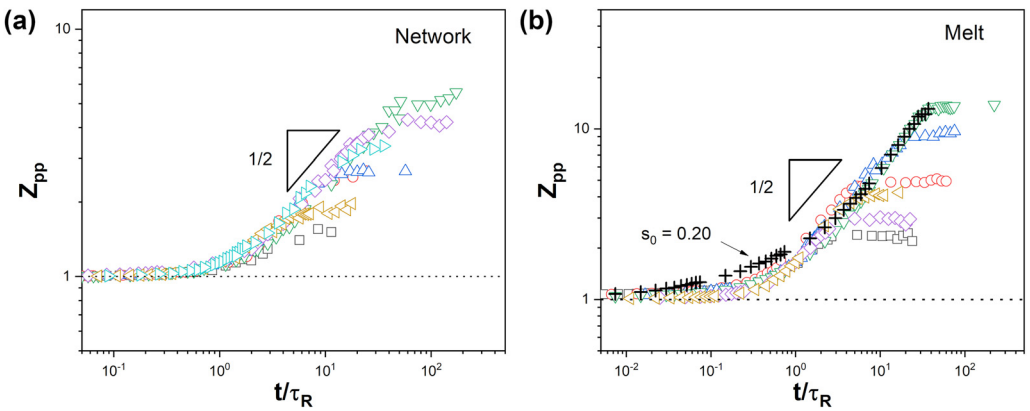


Fig. 10 Average number of entanglements per chain defined as $Z_{PP} \equiv \langle L_{PP}\rangle^2/\langle R^2\rangle$ against t/τ_R in (a) networks, and (b) melts. The legends are identical with Fig. 9. The cross scatters in (b) represent the PPA result when the initial configuration of the melt is less stretched (s_0 = 0.20).

In the transient regime, Z_{PP} in Fig. 10 proves that entanglements start recovering from the Rouse time in network and melt simulations, showing $Z_{PP} \sim (t/\tau_R)^{1/2}$. This result differs from what has been shown previously, looking at the transient perpendicular size in Fig. 5 and 6. Whereas in the network simulations, the time dependence of Z_{PP} is consistent with $\langle R_{yy}{}^2\rangle$, it was observed that the perpendicular sizes in the melts evolve as $\langle R_{yy}{}^2\rangle \sim t^{1/4}$ before full recovery, which are much slower than the increase of Z_{PP}. This difference between the evolution of $\langle R_{yy}{}^2\rangle$ and Z_{PP} in networks and melts is, in fact, in agreement with the theoretical picture proposed in Section II.2, according to which the creation of an entanglement along a test chain in a melt is also affected by the collective motion of the surrounding chains. Indeed, when the obstacles are fixed like our network simulation, the creation of entanglements only relies on the degree to which an individual chain explores the surrounding space. In contrast, when topological interaction originates from different chains as in the case of a melt, the number of new entanglements is determined by the increase of binary contacts. Since all the chains are recovered simultaneously, the creation of entanglements is thus faster than the single-chain case.

In Fig. 10(b), we also present the PPA result when the initial configuration of the melt is less stretched with s_0 = 0.20. The result proves that such an initial configuration is fully disentangled. Moreover, the change of Z_{PP} becomes independent of the initial configuration after the Rouse time τ_R, consistent with the discussion on stress relaxation in Fig. 14(b).

To highlight the inhomogeneous recovery of entanglements along the chain's contour, we analyze the distribution of kinks along the PP. The results are to be compared with the distribution of bond order parameters in Fig. 7, which describes the original chains before PPA. To describe the kinks, we divide the PP into N_b/N_{eb} vectors $\boldsymbol{u}_i$ and define the sharpness parameter: $k_i \equiv 0.5[1 - \langle\cos(\theta_i)\rangle]$, where θ_i is the angle between $\boldsymbol{u}_i$ and $\boldsymbol{u}_{i+1}$, as illustrated in Fig. 11(a). Here, we introduce a new quantity to describe the inhomogeneous recovery because it is more informative than the order parameter. In this definition, k_i = 0 means a straight line with no kink, and k_i = 1 means the neighboring vectors are opposite to each other (the sharpest kink). If the PP is considered as a worm-like chain, its persistent length will be $l_{PP} = -1/\ln(1 - 2k_i)$ in the unit of N_{eb} bonds. Examples of kinks' sharpness distribution in a network and a melt with similar equilibrium entanglement number (N_b/

 This journal is © The Royal Society of Chemistry 2026

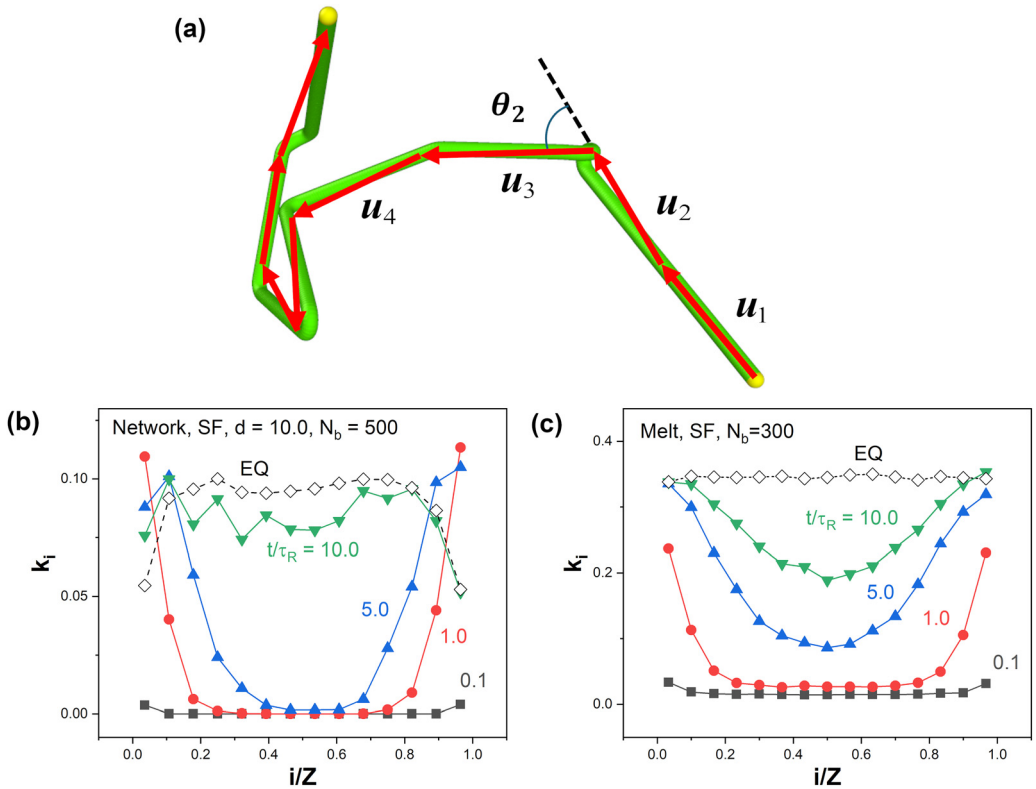


Fig. 11 (a) Snapshot of a single PP, which is divided into N_b/N_{eb} vectors. Distribution of kinks' sharpness along the chain's contour $k_i \equiv 0.5[1 - \langle\cos(\theta_i)\rangle]$ at different time scales in (b) a network and (c) a melt with similar number of entanglements per chain.

$N_{eb} \approx 15$) are presented in Fig. 11(b) and (c), respectively. Compared to Fig. 7 which reveals the structural inhomogeneity at the retraction stage when $t \ll \tau_R$, the kink distribution function in Fig. 11 better describes the entanglement property at the reorientation stage.

In Fig. 11(b), the equilibrium values of k_i in a network are much smaller than expected, suggesting that the persistent length of PP ($l_{PP} \approx 4.84$) is much larger than the estimation from network strand length. This is another way of showing the smaller entanglement number from PPA in networks, in addition to the effective number of Kuhn segments Z_{PP} as discussed in Fig. 10(a). In terms of dynamic mode, when $t \ll \tau_R$, there are no kinks along the PP in the two systems. A melt starts differing from a network at time $t \approx \tau_R$, when some kinks can be identified in the regime near chain ends, but not in the strand in the middle. In a network, the sharpness of kinks can reach a similar level as the equilibrium state, which means the same magnitude of confinement. In contrast, the kinks in a melt at $t \approx \tau_R$ are much smoother than the equilibrium ones. It means at this moment, the effective tube diameter, or saying the persistent length of PP, is much larger than the equilibrium value. We consider the two observations in the melt, including the absence of kinks in the chain's interior when $t \ll \tau_R$ and the higher smoothness at $t \approx \tau_R$, as proof of our theoretical assumption in Fig. 2(b). That is, at the onset of topological interaction, a terminal strand cannot form effective entanglement with the interior parts of other chains, and the entanglements between terminal strands have weaker confinement effect.

When $t > \tau_R$, reentanglement dynamics in a melt are more distinguishable from a network. For the network simulation as shown in Fig. 11(b), we can see that the kinks gradually "diffuse" from the extremity to the interior part. New kinks will not be created along the probe chain until the neighboring strand closer to the chain end becomes entangled with the network. However, when we examine the same time scale in a melt as presented in Fig. 11(c), an interior strand can form a kink without waiting for the full relaxation of the terminal strands. It suggests that entanglements are created between a terminal strand and an interior strand of another chain. Meanwhile, the sharpness of kinks in the terminal strand increases with time. This phenomenon indicates the instant tube diameter is decreased as chains' configurations are recovered, which does not exist in network simulations. In summary, the detailed investigation into the properties of PPs and the thorough comparison between network and melts simulations well support our molecular picture of reentanglement dynamics in an entangled melt proposed in Section II of this work.

IV.3 Stress relaxation

The stress relaxation function is another important quantity to trace the dynamics of reentanglement, and it is directly related to rheological measurements in experiments. We measure the

extensional stress $\sigma_E \equiv \sigma_{xx} - \sigma_{yy}$, where $\sigma_{\alpha\beta}$ is the component of the stress tensor including the contributions from kinetic energy, bonded and non-bonded interactions. The absolute value of stress is meaningless for network simulations because it depends on the size of the simulation. Thus, we focus on the dimensionless quantity $\sigma_E/\rho kT$, where ρ is the number density of beads. This quantity is useful because it represents the instant tension along the chain in a highly orientated state, based on the Kramer's expression of stress: $\sigma_E/\rho kT \approx f_t l_b/kT$. Thus, it is easy to estimate the level of non-Gaussian elasticity from the reduced stress. The onset of non-Gaussian stretch is $f_t b/kT \approx 1$, which means $\sigma_E/\rho kT \approx l_b/b \approx 0.30$ for a semiflexible chain and 0.56 for a flexible chain. The initial configurations of our network simulations have $\sigma_E/\rho kT \approx 20$, representing a strong non-Gaussian regime. The melt simulation with the initial bond orientation s_0 = 0.90 corresponds to the initial stresses $\sigma_E/\rho kT \approx 10.0$. The extensional stresses as a function of time are compared with the normalized linear relaxation modulus $G_0(t)/\rho kT$ with a prefactor, where the shear modulus is calculated from the time correlation function of stress component under equilibrium: $G_0(t) \equiv V/kT\langle\sigma_{xy}(t)\sigma_{xy}(0)\rangle$, with V is the volume of the simulation box. To reduce statistical noise, $G_0(t)$ in a network simulation is evaluated from the time correlation function of bond orientation tensor, with an appropriate shift factor applied, following the method by Cao and Likhtman.[62]

The simulation data in networks are shown in Fig. 12(a) and (b). First, the linear relaxation modulus in our network simulations exhibits the typical features of entangled dynamics: Rouse-like and chain-length independent relaxation $G_0 \sim t^{-1/2}$ when $t \ll \tau_e$, and a plateau regime when $\tau_e \ll t \ll \tau_d$. In Fig. 12(b), the height of plateau is elevated with the decrease of the network mesh size. The transient extensional stress also exhibits a Rouse-like ramp at the first step of relaxation. This regime is independent of the network mesh size and overlaps with the relaxation in a free space, as shown in Fig. 12(b). Fig. 12(c) suggests the Rouse time τ_R is the characteristic time scale of stress relaxation in the Rouse ramp regime. The relaxation of stress can be compared to that of $\langle R_x\rangle/L$ in Fig. 5(c), which does not exhibit a Rouse ramp. To explain the Rouse ramp observed in extensional stress, we can refer to the stress-optical coefficient: $\alpha_{SO} \equiv \sigma_E/\rho kT/s$, where s is the bond order parameter as mentioned previously. The corresponding data are presented in Fig. 13(a). This figure shows that the coefficient α_{SO} exhibits universal relaxation with respect to the Rouse time τ_R: $\alpha_{SO} \sim (t/\tau_R)^{-1/2}$. Moreover, α_{SO} becomes constant when $t > \tau_R$, indicating a Gaussian chain elasticity is recovered. Thus, the Rouse ramp observed in $\sigma_E/\rho kT$ results from the one-dimensional non-Gaussian to Gaussian elasticity transition along the chain contour. Because the non-Gaussian Rouse ramp persists up to τ_R, the elastic plateau of extensional stress can only be found in the regime of $\tau_R < t < \tau_d$. With a

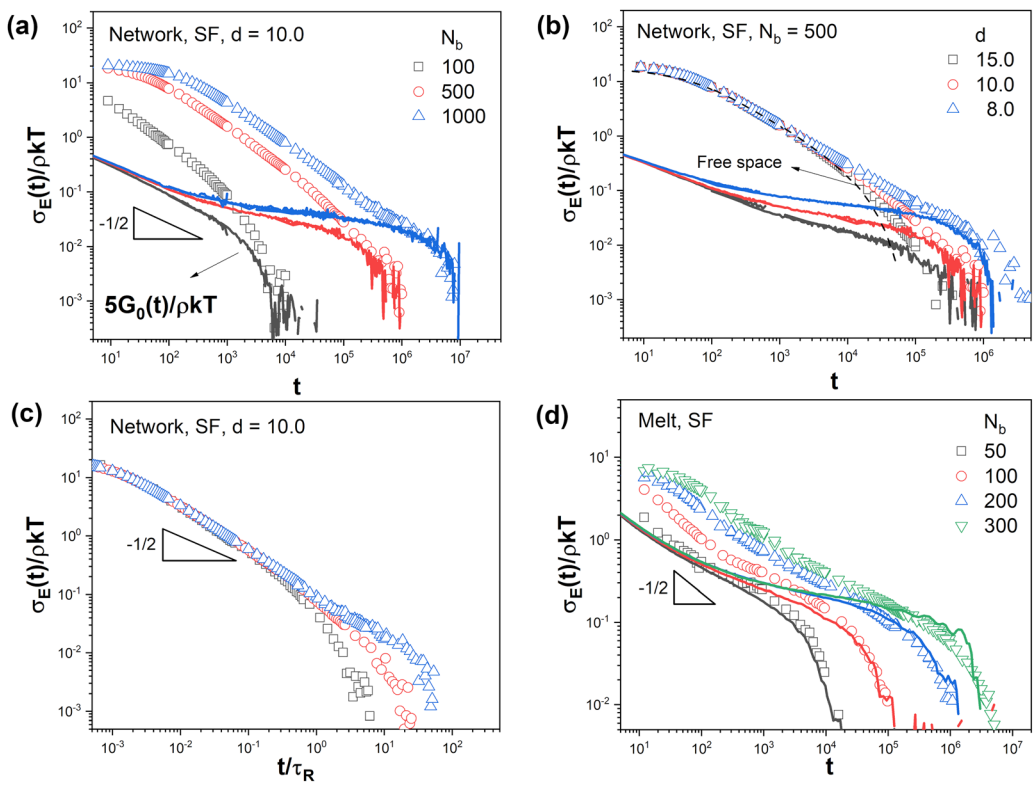


Fig. 12 Relaxation of normalized extensional stress $\sigma_E/\rho kT$ for (a) probe chains of different lengths in the same network (d = 10.0), and (b) the same probe chain (N_b = 500) in different networks. The transient extensional stresses are compared with the normalized linear relaxation modulus $G_0(t)/\rho kT$ multiplied with a prefactor of 5. (c) The same stress data in (a) against the normalized time t/τ_R. (d) Stress relaxation in melts of different chain lengths.

 This journal is © The Royal Society of Chemistry 2026

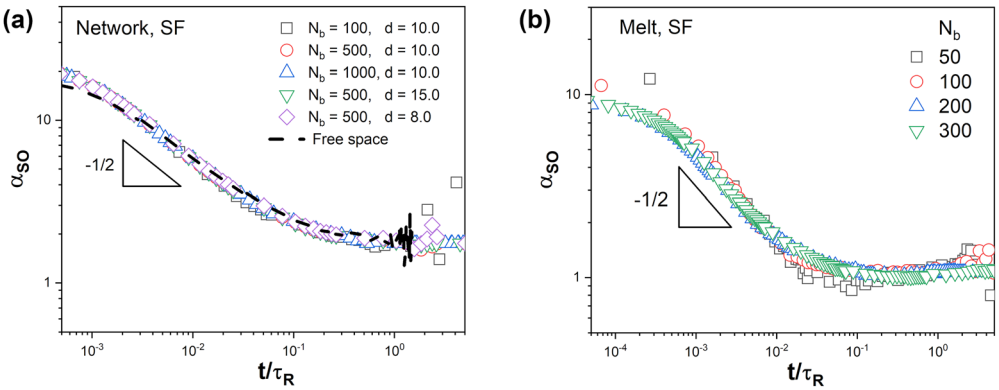


Fig. 13 Stress-optical coefficient α_{SO} defined as the ratio of normalized extensional stress to the bond order parameter for reentanglement dynamics in (a) networks and (b) melts.

prefactor of 5, the terminal relaxation of σ_E overlays well with that of linear relaxation modulus G_0, proving the consistency between equilibrium and reentanglement dynamics in network simulations.

Stress relaxation from melt simulations as shown in Fig. 12(d) exhibits very similar behavior as network simulations. It also starts with a Rouse ramp, due to the non-Gaussian to Gaussian transition as confirmed from the stress-optical coefficient α_{SO} in Fig. 13(b). It must be noted that the Rouse time is sufficient to overlay the data of α_{SO} of the melts. Our results are also close to the experimental data of stress relaxation after uniaxial extension[63] (after choosing the moment of flow cessation as $t = 0$, as replotted by Wu *et al.*[64]) The terminal stress relaxation from a highly stretched state also aligns well with that of the linear relaxation modulus, in agreement with our theoretical prediction that the full relaxation time is unaltered from the equilibrium disentanglement time despite the change of relaxation path way.

We also examine stress relaxation when the initial levels of chain stretching are changed. This corresponds to the case of relaxation after subjecting to different flow rates. In Fig. 14(a) for network simulations, the initial extensional stress reduces from $\sigma_E/\rho kT \approx 20$ to 0.45 when the bond order parameter in the initial configuration changes from $s_0 = 1$ to 0.20. The initial stress of the melt data in Fig. 14(b) changes to a similar magnitude with the decrease of initial stretching. The comparison shows that the effect of initial configurations persists up to the Rouse time τ_R. If the initial configuration does not have non-Gaussian elasticity, the extensional stress $\sigma_E/\rho kT$ will not exhibit a Rouse ramp but rather a plateau regime.

In summary, there are two main messages from the current section about stress relaxation: one is that the Rouse ramp of extensional stress when $t < \tau_R$ is due to the non-Gaussian to Gaussian elasticity transition, supported by the Rouse-like relaxation of the stress-optical coefficient. This mechanism is also highlighted when comparing the relaxation from different initial configurations. The other is that stress relaxation can hardly distinguish the reentanglement dynamics of a melt from a probe in a network. This observation highlights the importance of interrupted flow measurement, which better captures the level of recovery at different stages from the transient response on a newly imposed flow.

V Conclusion

In conclusion, the current work systematically compared the relaxation of a highly stretched polymer chain in fixed networks

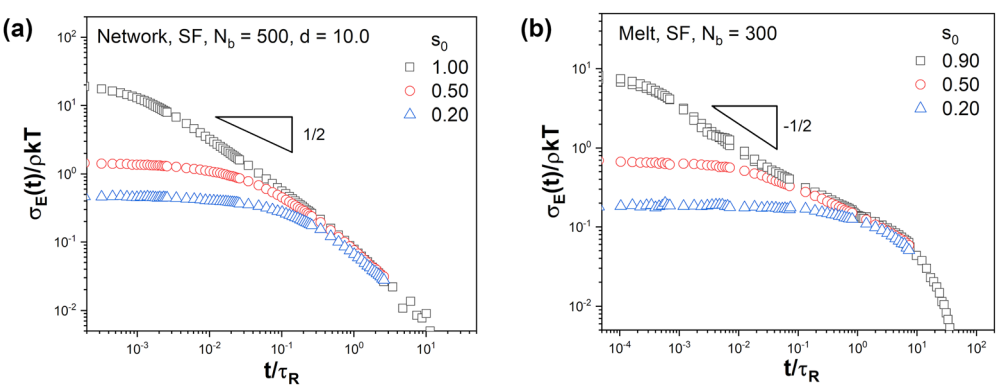


Fig. 14 Relaxation of normalized extensional stress $\sigma_E/\rho kT$ starting from the different initial configurations (level of stretching indicated by the bond order parameter s_0) in (a) network simulations and (b) melt simulations.

and polymer melts which are well entangled under equilibrium but fully disentangled in their initial configurations, from theoretical analysis and MD simulations. In the theoretical part of this work, we reviewed the prediction of the classic reptation theory which assumes a space with fixed obstacles. Then, we explained the reentanglement dynamics of a highly stretched melt differs from the single-chain scenario in two aspects: one is that a polymer starts feeling the onset of entanglement at the length scale of a "just-entangled strand" size $\xi_{je} \cong aZ^{1/3}$ where a is the equilibrium tube diameter and Z is the equilibrium entanglement number. The other is that after the retraction of PP characterized by the Rouse time τ_R, the self-consistent expression between the perpendicular size $\langle {R_{yy}}^2 \rangle$ and the instant entanglement number results in the time dependence $\langle {R_{yy}}^2 \rangle \sim t^{1/4}$, in comparison to the second Rouse-like regime $\langle {R_{yy}}^2 \rangle \sim t^{1/2}$ in networks. Despite the change of relaxation pathway, the full recovery time of a melt still agrees with the disentanglement time τ_d in our theoretical prediction, consistent with experimental observations from interrupted shear measurement.

The theoretical predictions were examined from two sets of simulation data. In the first set of data, we simulated single-chain Langevin dynamics in fixed networks. Not only the equilibrium dynamics but also the reentanglement dynamics from a fully stretched configuration from our simulations were found quantitatively consistent with the classic reptation theory. The main feature of reentanglement dynamics in our network simulations was that the perpendicular size $\langle {R_{yy}}^2 \rangle$ exhibited an unambiguous second Rouse-like regime in the regime $t \gg \tau_R$. The other set of simulation data of polymer melts starting from highly stretched configurations showed qualitatively different behaviors as network simulations in terms of the recovery of perpendicular size, although they were almost indistinguishable from equilibrium dynamics. The two-power-law behavior, full recovery time extracted from the simulation data of $\langle {R_{yy}}^2 \rangle$ were found to agree well with the theoretical predictions. The length scales of entanglement onset were found to be close to the just-entangled strand length as defined in the theoretical part. The distribution functions of bond order parameters proved inhomogeneous relaxation during reentanglement dynamics. The PPA in the two systems showed that in a melt, the effective entanglement number relies on the binary contact of the polymer chains, and thus it grows fast with time compared to the perpendicular size. Whereas the time-dependence of the two quantities were found to be identical in network simulations, which can be described as the single-chain event. The development of kinks along the PPs proved that reentanglement occurs differently along the chain's contour and a melt can exhibit a more uniform recovery of entanglements at the reorientation stage compared to the probe chain in a network. In terms of stress relaxation, the network and melt simulations behaved similarly, showing that the reconstruction of entanglement network in a relaxing melt does not play a significant role in stress relaxation within our parameter range.

Overall, the theoretical framework and simulation results presented in this work provide improved understanding of experimental observations on reentanglement dynamics and offer new insights into single-chain behavior across different time scales out of equilibrium. These findings may also facilitate the development of new molecular models for the nonlinear rheology of entangled polymers, a field that continues to present significant challenges.

Conflicts of interest

There is no conflicts to declare.

Data availability

Supplementary information (SI), including the check of simulation methods, equilibrium dynamics, entanglement times in network simulations, evolution of radius of gyration, reentanglement dynamics of flexible chains, and monomer–monomer pair correlation functions in melt simulations. See DOI: https://doi.org/10.1039/d6sm00446f.

The data related to the figures will be posted in the repository of UCLouvain. Simulation input files, analysis scripts, and processed datasets supporting the figures are openly available at repository DOI: https://doi.org/10.14428/DVN/IL1MIY. Raw simulation trajectories are available from the corresponding author upon reasonable request due to file size constraints.

Acknowledgements

We thank the Excellence of Science programme (grant EOS 40007519) from the FWO and F.R.S.-FNRS for financial support. E. V. R. is Director of Research of the FRS-FNRS. We would like to express our sincere gratitude to Prof. Michael Rubinstein for his invaluable guidance and support throughout our research projects. His exceptional expertise, his boundless enthusiasm for scientific questions in polymer physics and his kindness make working with him a truly enriching experience. We wish him a very happy birthday and many more years of research and friendship.

References

1 M. Doi and S. F. Edwards, *The theory of polymer dynamics*. Oxford University Press, New York, 1986.
2 M. Rubinstein and R. H. Colby, *Polymer Physics*, Oxford University Press, New York, 2003.
3 M. E. Mackay, The importance of rheological behavior in the additive manufacturing technique material extrusion, *J. Rheol.*, 2018, **62**(6), 1549–1561.
4 T. J. Coogan and D. O. Kazmer, Prediction of interlayer strength in material extrusion additive manufacturing, *Addit. Manuf.*, 2020, **35**, 101368.
5 X. Gao, S. Qi, X. Kuang, Y. Su, J. Li and D. Wang, Fused filament fabrication of polymer materials: A review of interlayer bond, *Addit. Manuf.*, 2021, **37**, 101658.

 This journal is © The Royal Society of Chemistry 2026

6 K. Cui, Z. Ma, N. Tian, F. Su, D. Liu and L. Li, Multiscale and Multistep Ordering of Flow-Induced Nucleation of Polymers, *Chem. Rev.*, 2018, **118**(4), 1840–1886.

7 C. Nie, F. Peng, R. Cao, K. Cui, J. Sheng, W. Chen and L. Li, Recent progress in flow-induced polymer crystallization, *J. Polym. Sci.*, 2022, **60**(23), 3149–3175.

8 C. Baig, V. G. Mavrantzas and M. Kroger, Flow Effects on Melt Structure and Entanglement Network of Linear Polymers: Results from a Nonequilibrium Molecular Dynamics Simulation Study of a Polyethylene Melt in Steady Shear, *Macromolecules*, 2010, **43**(16), 6886–6902.

9 R. Everaers, S. K. Sukumaran, G. S. Grest, C. Svaneborg, A. Sivasubramanian and K. Kremer, Rheology and microscopic topology of entangled polymeric liquids, *Science*, 2004, **303**(5659), 823–826.

10 M. Kroger, Shortest multiple disconnected path for the analysis of entanglements in two- and three-dimensional polymeric systems, *Comput. Phys. Commun.*, 2005, **168**(3), 209–232.

11 C. Y. Liu and H. Morawetz, Kinetics of the unfolding of collapsed polystyrene chains above the glass transition temperature, *Macromolecules*, 1988, **21**(2), 515–518.

12 C. G. Robertson, S. Warren, D. J. Plazek and C. M. Roland, Reentanglement Kinetics in Sheared Polybutadiene Solutions, *Macromolecules*, 2004, **37**(26), 10018–10022.

13 D. Roy and C. M. Roland, Reentanglement Kinetics in Polyisobutylene, *Macromolecules*, 2013, **46**(23), 9403–9408.

14 M. A. Galvani Cunha, P. D. Olmsted and M. O. Robbins, Probing the nonequilibrium dynamics of stress, orientation, and entanglements in polymer melts with orthogonal interrupted shear simulations, *J. Rheol.*, 2022, **66**(3), 619–637.

15 G. Ianniruberto and G. Marrucci, On compatibility of the Cox-Merz rule with the model of Doi and Edwards, *J. Non-Newtonian Fluid Mech.*, 1996, **65**(2), 241–246.

16 R. S. Graham, A. E. Likhtman, T. C. B. McLeish and S. T. Milner, Microscopic theory of linear, entangled polymer chains under rapid deformation including chain stretch and convective constraint release, *J. Rheol.*, 2003, **47**(5), 1171–1200.

17 A. E. Likhtman and R. S. Graham, Simple constitutive equation for linear polymer melts derived from molecular theory: Rolie-Poly equation, *J. Non-Newtonian Fluid Mech.*, 2003, **114**(1), 1–12.

18 D. W. Mead, R. G. Larson and M. Doi, A Molecular Theory for Fast Flows of Entangled Polymers, *Macromolecules*, 1998, **31**(22), 7895–7914.

19 H. Taghipour, S. Costanzo, D. Vlassopoulos, E. V. Ruymbeke and L. G. D. Hawke, Entangled linear polymers in fast shear flows: Comparison of tube-model predictions and experimental data, *J. Rheol.*, 2021, **65**(6), 1111–1137.

20 M. Andreev, R. N. Khaliullin, R. J. A. Steenbakkers and J. D. Schieber, Approximations of the discrete slip-link model and their effect on nonlinear rheology predictions, *J. Rheol.*, 2013, **57**(2), 535–557.

21 T. Yaoita, T. Isaki, Y. Masubuchi, H. Watanabe, G. Ianniruberto and G. Marrucci, Primitive Chain Network Simulation of Elongational Flows of Entangled Linear Chains: Stretch/Orientation-induced Reduction of Monomeric Friction, *Macromolecules*, 2012, **45**(6), 2773–2782.

22 G. Ianniruberto and G. Marrucci, Convective constraint release (CCR) revisited, *J. Rheol.*, 2014, **58**(1), 89–102.

23 B. E. Dolata and P. D. Olmsted, A thermodynamically consistent constitutive equation describing polymer disentanglement under flow, *J. Rheol.*, 2022, **67**(1), 269–292.

24 B. E. Dolata, M. A. Galvani Cunha, T. O'Connor, A. Hopkins and P. D. Olmsted, Entanglement Kinetics in Polymer Melts Are Chemically Specific, *ACS Macro Lett.*, 2024, **13**(7), 896–902.

25 M. Boudaghi, M. H. Nafar Seddashti, B. J. Edwards and B. Khomami, Elucidating the role of network topology dynamics on the coil-stretch transition hysteresis in extensional flow of entangled polymer melts, *J. Rheol.*, 2022, **66**(3), 551–569.

26 A. Córdoba, D. Becerra and J. D. Schieber, Reëntanglement Dynamics in Polymer Melts Can Be Explained by Fast Dangling End Retraction without Resorting to Nonuniversality, *ACS Macro Lett.*, 2025, **14**(3), 385–390.

27 Y. H. Lin, Number of entanglement strands per cubed tube diameter, a fundamental aspect of topological universality in polymer viscoelasticity, *Macromolecules*, 1987, **20**(12), 3080–3083.

28 T. A. Kavassalis and J. Noolandi, A new theory of entanglements and dynamics in dense polymer systems, *Macromolecules*, 1988, **21**(9), 2869–2879.

29 L. J. Fetters, D. J. Lohse, D. Richter, T. A. Witten and A. Zirkel, Connection between Polymer Molecular Weight, Density, Chain Dimensions, and Melt Viscoelastic Properties, *Macromolecules*, 1994, **27**(17), 4639–4647.

30 R. Everaers, H. A. Karimi-Varzaneh, F. Fleck, N. Hojdis and C. Svaneborg, Kremer–Grest Models for Commodity Polymer Melts: Linking Theory, Experiment, and Simulation at the Kuhn Scale, *Macromolecules*, 2020, **53**(6), 1901–1916.

31 Y. Matsumiya and H. Watanabe, Non-Universal Features in Uniaxially Extensional Rheology of Linear Polymer Melts and Concentrated Solutions: A Review, *Prog. Polym. Sci.*, 2021, **112**, 101325.

32 G. Ianniruberto, G. Marrucci and Y. Masubuchi, Melts of Linear Polymers in Fast Flows, *Macromolecules*, 2020, **53**(13), 5023–5033.

33 M. Dalne, S. Costanzo, K. Peponaki, N. Jiang, S. Alexandris, N. Grizzuti, D. Vlassopoulos, M. Rubinstein and E. van Ruymbeke, Nonlinear Shear Rheology of Unentangled Polymer Melts, *Macromolecules*, 2025, **58**(14), 7062–7083.

34 N. Jiang, Potential Universal Extensional Rheology in Concentrated Polymeric Liquids, *Macromolecules*, 2024, **57**(11), 5520–5532.

35 N. Jiang and E. van Ruymbeke, Variation of Spring Stiffness, Monomeric Friction, and Brownian Intensity in the Simulation System of Unentangled Melt under Steady Flow, *Macromolecules*, 2023, **56**(8), 2911–2929.

36 J. Farago, A. Semenov, H. Meyer, J. Wittmer, A. Johner and J. Baschnagel, Mode-coupling approach to polymer diffusion

in an unentangled melt. I. The effect of density fluctuations, *Phys. Rev. E:Stat., Nonlinear, Soft Matter Phys.*, 2012, **85**(5), 051806.
37 K. S. Schweizer, Microscopic theory of the dynamics of polymeric liquids: General formulation of a mode–mode-coupling approach, *J. Chem. Phys.*, 1989, **91**(9), 5802–5821.
38 J. Farago, H. Meyer, J. Baschnagel and A. N. Semenov, Mode-coupling approach to polymer diffusion in an unentangled melt. II. The effect of viscoelastic hydrodynamic interactions, *Phys. Rev. E: Stat., Nonlinear, Soft Matter Phys.*, 2012, **85**(5), 051807.
39 J. Farago, H. Meyer and A. N. Semenov, Anomalous Diffusion of a Polymer Chain in an Unentangled Melt, *Phys. Rev. Lett.*, 2011, **107**(17), 178301.
40 N. Jiang, Diffusion of a Polymer Tracer in an Unentangled Matrix, *Macromolecules*, 2026, **59**(1), 587–600.
41 T. Ge, S. Panyukov and M. Rubinstein, Self-Similar Conformations and Dynamics in Entangled Melts and Solutions of Nonconcatenated Ring Polymers, *Macromolecules*, 2016, **49**(2), 708–722.
42 D. Parisi, S. Costanzo, Y. Jeong, J. Ahn, T. Chang, D. Vlassopoulos, J. D. Halverson, K. Kremer, T. Ge, M. Rubinstein, G. S. Grest, W. Srinin and A. Y. Grosberg, Nonlinear Shear Rheology of Entangled Polymer Rings, *Macromolecules*, 2021, **54**(6), 2811–2827.
43 J. D. Halverson, W. B. Lee, G. S. Grest, A. Y. Grosberg and K. Kremer, Molecular dynamics simulation study of nonconcatenated ring polymers in a melt. II. Dynamics, *J. Chem. Phys.*, 2011, **134**(20), 204905.
44 B. Mei, G. S. Grest, S. Liu, T. C. O'Connor and K. S. Schweizer, Unified understanding of the impact of semiflexibility, concentration, and molecular weight on macromolecular-scale ring diffusion, *Proc. Natl. Acad. Sci. U.S.A.*, 2024, **121**(31), e2403964121.
45 P. G. de Gennes, Remarks on entanglements and rubber elasticity, *J. Phys., Lett.*, 1974, **35**(9), 133–134.
46 M. Rubinstein and R. H. Colby, Self-consistent theory of polydisperse entangled polymers: Linear viscoelasticity of binary blends, *J. Chem. Phys.*, 1988, **89**(8), 5291–5306.
47 T. Shahid, C. Clasen, F. Oosterlinck and E. van Ruymbeke, Diluting Entangled Polymers Affects Transient Hardening but Not Their Steady Elongational Viscosity, *Macromolecules*, 2019, **52**(6), 2521–2530.
48 J. Klein, Effect of matrix molecular weight on diffusion of a labeled molecule in a polymer melt, *Macromolecules*, 1981, **14**(2), 460–461.
49 P. F. Green and E. J. Kramer, Matrix effects on the diffusion of long polymer chains, *Macromolecules*, 1986, **19**(4), 1108–1114.
50 F. Brochard-Wyart, A. Ajdari, L. Leibler, M. Rubinstein and J. L. Viovy, Dynamics of stars and linear chains dissolved in a polymer melt, *Macromolecules*, 1994, **27**(3), 803–808.
51 A. P. Thompson, H. M. Aktulga, R. Berger, D. S. Bolintineanu, W. M. Brown, P. S. Crozier, P. J. in't Veld, A. Kohlmeyer, S. G. Moore, T. D. Nguyen, R. Shan, M. J. Stevens, J. Tranchida, C. Trott and S. J. Plimpton, LAMMPS – a flexible simulation tool for particle-based materials modeling at the atomic, meso, and continuum scales, *Comput. Phys. Commun.*, 2022, **271**, 108171.
52 D. Shirvanyants, S. Panyukov, Q. Liao and M. Rubinstein, Long-Range Correlations in a Polymer Chain Due to Its Connectivity, *Macromolecules*, 2008, **41**(4), 1475–1485.
53 A. Baumgärtner and M. Muthukumar, A trapped polymer chain in random porous media, *J. Chem. Phys.*, 1987, **87**(5), 3082–3088.
54 P. G. de Genne, Reptation of a Polymer Chain in the Presence of Fixed Obstacles, *J. Chem. Phys.*, 1971, **55**(2), 572–579.
55 S. F. Edwards and M. Muthukumar, The size of a polymer in random media, *J. Chem. Phys.*, 1988, **89**(4), 2435–2441.
56 A. Stukowski, Visualization and analysis of atomistic simulation data with OVITO–the Open Visualization Tool, *Modell. Simul. Mater. Sci. Eng.*, 2010, **18**(1), 015012.
57 G. S. Grest, Communication: Polymer entanglement dynamics: Role of attractive interactions, *J. Chem. Phys.*, 2016, **145**(14), 141101.
58 C. Svaneborg and R. Everaers, Characteristic Time and Length Scales in Melts of Kremer–Grest Bead–Spring Polymers with Wormlike Bending Stiffness, *Macromolecules*, 2020, **53**(6), 1917–1941.
59 M. Rubinstein and S. P. Obukhov, Memory effects in entangled polymer melts, *Phys. Rev. Lett.*, 1993, **71**(12), 1856–1859.
60 M. Kröger, J. D. Dietz, R. S. Hoy and C. Luap, The Z1+ package: Shortest multiple disconnected path for the analysis of entanglements in macromolecular systems, *Comput. Phys. Commun.*, 2023, **283**, 108567.
61 D. Chen, S. Panyukov, L. Sapir and M. Rubinstein, Elasticity of Slide-Ring Gels, *ACS Macro Lett.*, 2023, **12**(3), 362–368.
62 J. Cao and A. E. Likhtman, Time-Dependent Orientation Coupling in Equilibrium Polymer Melts, *Phys. Rev. Lett.*, 2010, **104**(20), 207801.
63 Q. Huang and H. K. Rasmussen, Stress relaxation following uniaxial extension of polystyrene melt and oligomer dilutions, *J. Rheol.*, 2016, **60**(3), 465–471.
64 L.-F. Wu, L.-F. Mao and Z. Wang, Effective Entanglement and Constraint Release in Deformed Polymer Melts, *Macromolecules*, 2024, **57**(7), 3202–3211.

 This journal is © The Royal Society of Chemistry 2026